An integrated computational framework for structural optimization of prestressed concrete structures with 3D-printed formwork

Emad Shakur[a,*], Oded Amir[a]

[a]*Technion – Israel Institute of Technology, Technion City, Haifa, 3200003, Israel*

Abstract

In this paper, we present an integrated computational framework for the optimal design of post-tensioned concrete structures, assembled from segments that are composed of printed formwork and complementary casting. The framework hinges upon shape optimization of B-spline surfaces that parameterize castable concrete members, and accounts for both the load-balancing stage and the service stage, commonly referred to in prestressed concrete design. Buildability of the formwork is guaranteed by separating the geometry of the printed toolpath and imposing a set of stress constraints according to the material properties of the fresh concrete. Numerical results show how the capacity of the fresh concrete and fabrication parameters affect the outcome of shape optimization, and how the optimizer successfully finds geometrical forms that are buildable. This paves the way towards a holistic, seamless design-for-manufacturing approach in 3D concrete printing.

Keywords: 3D printed concrete, shape optimization, prestressed concrete, buildability, embodied CO_2

1. Introduction

The cement industry is a major contributor to global CO_2 emissions (Andrew, 2019), prompting urgent calls to reduce cement usage in construction until scalable and truly eco-friendly alternatives emerge. One effective route is to minimize concrete consumption through structural optimization. However, conventional construction methods make it difficult to realize highly optimized, complex shapes: creating tailor-made formwork is labor-intensive, costly, and time-consuming, thus it can eliminate the gains achieved from optimizing material usage.

Additive manufacturing (AM), in particular 3D printing of cementitious materials—commonly referred to as 3D concrete printing (3DCP)—may offer a promising alternative. By enabling the direct fabrication of complex geometries without the need for traditional temporary formwork, 3DCP has the potential to reduce waste, accelerate construction, and expand the possibilities for

*Corresponding author: semad@technion.ac.il

creating optimized structural forms. Recent studies reviewing the state of structural 3DCP in both research and industry highlight its rapid growth across hundreds of small- and full-scale projects (Hasani and Dorafshan, 2024).

While the vast majority of applications of 3DCP demonstrate the rapid and accurate construction of vertical components—primarily walls—the fabrication of horizontal members that act in bending remains far less explored. Addressing this gap requires overcoming both structural demands and fabrication constraints. Horizontally spanning elements must resist significant bending moments, which typically necessitates the use of continuous reinforcement or prestressing.

One strategy for avoiding bending is to employ compression-only geometries, which align naturally with the material behavior of unreinforced printed concrete. This approach has been demonstrated at full scale, most notably in the Striatus bridge, a compression-only arch constructed from dry-assembled printed concrete voussoirs without reinforcement (Bhooshan et al., 2022). A related concept is the FloatArch girder, in which printed segments are shaped to follow the flow of compression forces and are assembled using external post-tensioning to create a reusable structural member (Li et al., 2024).

In the case of beams and slabs, which must resist significant bending moments, compression-only behavior can be achieved by prestressing. Prestressing enables these members to act more like compression-dominated structures while maintaining relatively slender profiles. In the context of 3DCP, this has motivated the use of post-tensioning to assemble printed segments into continuous members, remaining predominantly in compression throughout service life. An early demonstration was the printed pedestrian bridge by Salet et al. (2018), fabricated in segments using a predefined toolpath and subsequently post-tensioned. Segmental fabrication in 3DCP naturally accommodates this approach, since cables can be threaded through cavities formed between printed segments to tighten them together. In addition, prestressing applied along the printing direction helps clamp layers together and compensate for weak interlayer bonding, that affects resistance to shear. Recent experimental studies have further examined the feasibility of prestressing in 3D printed horizontal elements. Gebhard et al. (2021) confirmed the viability of prestressed segmental components using external or internal tendons, and Coward and Sørensen (2023) showed that post-tensioning can significantly improve the flexural performance of printed beams.

Building on the optimization procedures for prestressed designs developed by Amir and Shakour (2018), Vantyghem et al. (2020) designed, fabricated, and tested a post-tensioned beam by translating two-dimensional optimized topologies into manufacturable three-dimensional components through CAD-based interpretation, demonstrating the potential of integrating optimization into the digital fabrication workflow of 3DCP. To reduce manual interpretation between two- and three-dimensional representations and to enable a wider range of geometries, Shakur

et al. (2024) advanced the optimization methodology by generalizing it to fully free-formed three-dimensional prestressed beams and slabs. Yet, despite these advances, the fabrication of geometrically free-formed optimized designs remains challenging, underscoring the need to align optimization procedures with current 3DCP capabilities and to embed manufacturability constraints directly into the design process.

One fabrication route for 3D printed horizontal elements relies on hybrid construction, in which printed components are combined with conventionally cast concrete. In such systems, 3D printing is used primarily to create geometrically complex formwork that would be difficult or uneconomical to build using traditional methods, while the cast concrete provides the necessary mechanical performance and structural continuity. This concept was first explored for vertical load-bearing elements, such as printed stay-in-place formwork for reinforced concrete walls and columns (Anton et al., 2021; Zhu et al., 2021; Chen et al., 2023). This progress has driven ongoing investigations into the quality of bonding between printed formwork and poured concrete (Wang et al., 2022; Chen et al., 2023; Qiu et al., 2024; Bai et al., 2025). Extending the approach to horizontally spanning members is a natural progression, as hybridization can mitigate the bending-related limitations of unreinforced printed concrete while preserving the geometric freedom offered by 3DCP.

Recent work has advanced 3D-printed stay-in-place formwork for horizontally spanning elements. Raza et al. (2025a) studied load transfer in thin printed ribbed slabs under end-anchorage post-tensioning, identifying key structural behaviors. Sakha et al. (2026) developed an optimization and assessment framework showing that post-tensioned printed formwork can support self-weight and cast toppings without temporary shoring. Flexural tests by Raza et al. (2025b) further demonstrated that such systems can participate structurally once filled and prestressed. These studies showcase post-tensioned 3D-printed formwork as a viable construction process for optimized horizontal elements.

A key challenge in 3DCP is ensuring that fresh concrete can sustain its own self-weight during printing. To address this, several buildability models have been developed (Mechtcherine et al., 2020; Mohan et al., 2021). Early analytical work established stability criteria based on the evolving strength of fresh concrete (Roussel, 2018; Wangler et al., 2016), highlighting the importance of time-dependent thixotropy as lower layers accumulate load. Simplified yield-stress evolution laws enabled practical estimation of failure during printing and feasible build rates (Perrot et al., 2015; Kruger et al., 2019, 2020). Subsequent studies introduced numerical models calibrated with time-dependent mechanical properties (Wolfs et al., 2018; Wolfs, 2019; Jayathilakage et al., 2020; Suiker, 2018). Voxelprint further advanced predictive capability through transient simulation of layer deposition and associated geometric instabilities (Vantyghem et al., 2021). More recently, Asaf et al. (2024a) proposed an integrated rheology-based design framework linking mix composition, printing parameters, and component geometry, offering a unified

approach for ensuring early-age stability.

Together, these developments reveal a clear trajectory: while 3DCP, prestressing, optimization, and hybrid casting each contribute important capabilities, they remain only partially integrated. Fully exploiting their combined potential requires design methods that simultaneously consider structural behavior, geometric freedom, material fresh-state limitations, and fabrication constraints. Motivated by this need, the present work introduces a comprehensive computational framework for the design optimization of post-tensioned concrete members, assembled from segments composed of printed stay-in-place formwork and complementary cast concrete. The framework rests on four pillars: (1) A geometry parameterization that enables optimization of the formwork's outer surface while ensuring castability; (2) A mathematical problem formulation that accounts for both the load-balancing stage, in which deformations due to self-weight, partial dead load, and prestressing are balanced, and the service stage, in which stiffness under the remaining dead and live loads is maximized; (3) Explicit geometric relations linking the formwork surface, tendon layout, and printable toolpath; and (4) Buildability constraints that ensure the formwork can be fabricated layer-by-layer under the limitations of the material's early-age strength evolution and of the printing system.

For the latter, we extend the buildability formulation of Mogra (2023), which is based on the lower-bound stability model of Kruger et al. (2019), enforcing layer-by-layer stress-based constraints throughout the simulated printing process to guarantee feasible fabrication. For the optimization, we represent the design by its outer surface using a B-spline parameterization and perform shape optimization directly on this surface. Recent work has also employed shape optimization in the context of 3D-printed concrete (Wan et al., 2025).

The remainder of this paper is organized as follows. In Section 2 we introduce the concept of post-tensioned concrete members with 3D-printed formwork. The design parameterization—based on optimizing the outer surface geometry of the formwork—is presented in Sections 3 and 4, followed by the procedure for generating printing toolpaths in Section 5. The governing equations, optimization problem formulation, and sensitivity analysis are detailed in Sections 6, 7, and 8. Several design examples are presented in Section 9 to demonstrate the proposed framework and concluding remarks are provided in Section 10.

2. Post-tensioned design with 3D-printed formwork

In this section, we present the details of the 3D-printed formwork approach and outline the key considerations that guided the proposed methodology. The central idea is to divide the post-tensioned design into consecutive fabrication stages: 3D printing of the formwork, casting and assembly by post-tensioning. To facilitate construction, the 3D-printed part is produced in segments, which are connected by post-tensioning cables running through the upper and lower chords of the design. The cables enable assembly of the segments and provide the prestressing

required to reduce displacements and stresses, as discussed in later sections.

The implementation of the combined printed-cast design requires adherence to specific geometrical constraints as well as practical construction considerations. These are presented below and are accompanied by illustrative examples in Figure 1 for clarity.

1. The upper loading plane is assumed to remain fixed throughout the optimization. This reflects realistic conditions in which the position of the applied loads cannot be altered. Accordingly, the optimization is applied only to the geometry below the fixed loading plane.

2. The cross-section of the 3D-printed toolpath is assumed to be rectangular, with width l_w and height l_h. An overlap of length l_o is introduced between toolpaths in successive layers and between adjacent toolpaths within the same layer, to ensure proper bonding.

3. The prestressing cables are positioned at a prescribed distance from the outer shape of the design. They are inserted through channels that are embedded within the 3D-printed part, defined by the geometry of the toolpaths. Each 3D-printed layer consists of three parallel toolpaths, with gaps introduced between the two inner paths to form the cable channels, as illustrated in Figure 1.

4. The toolpath generated within each layer must be continuous and free of self-intersections.

5. The formwork design must allow for proper placement of concrete to fill the interior of the prestressed structure. This requires keeping the upper part open to permit concrete pouring while ensuring that no blockages occur, so that the cast part is completely filled.

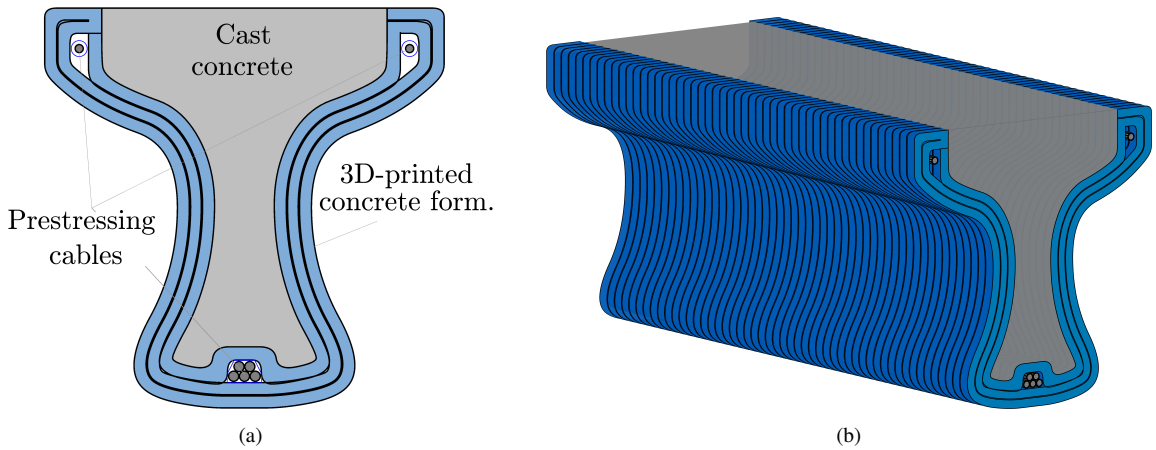

Figure 1: Overview of the design concept. (a) Cross-section consisting of 3D-printed formwork and casting. The 3D-printed formwork cross-section, referred to as a layer, consists of three parallel toolpaths with openings for the insertion of cables. The upper part is left open, without blockages, to allow the cast concrete to fill the interior. (b) A representative segment of a beam, designed according to the proposed approach.

3. B-Spline-based representations

The methodology in this study employs B-spline surfaces and curves to represent the geometry of post-tensioned beams and slabs. In this section, we provide a concise introduction to B-spline curves and surfaces, along with the essential functionality required in this work. For comprehensive coverage of spline-based modeling, the reader is referred to (Piegl and Tiller, 2012).

3.1. B-Spline curves and surfaces

B-splines are widely used in computer-aided design (CAD), due to their ability to represent curved geometries with high precision and smoothness. Their control parameters also offer an intuitive mechanism for adjusting the geometry, which makes them particularly suitable for geometrical modeling.

Starting with univariate B-splines, the parametric domain is partitioned into intervals defined by a knot vector, which is a non-decreasing sequence $\Xi = [\xi_1, \xi_2, \ldots, \xi_{,n+p+1}]$, $\xi_i \leq \xi_{i+1}$, where n is the number of basis functions and p is the polynomial degree. The knot vector is called *uniform* when all interior knot spans are equal, *open* when the first and last knots are repeated $(p + 1)$ times, and *open uniform* when both conditions are satisfied. The univariate B-spline basis functions $B_{i,p}(\xi)$ of degree p are defined recursively by the Cox–de Boor recursion (Piegl and Tiller, 2012). Given the basis functions, a univariate B-spline curve of degree p is expressed as

$$\mathbf{C}(\xi) = \sum_{i=1}^{n} B_{i,p}(\xi)\, \mathbf{P}_i, \tag{1}$$

where $\mathbf{P}_i \in \mathbb{R}^d$ are the control points that determine the curve's shape in the physical domain, and d denotes the dimension of the problem.

Extending this formulation to two parametric directions, bivariate B-spline surfaces are constructed as tensor products of univariate basis functions. Let $B_{i,p}(\xi)$ and $B_{j,q}(\eta)$ denote the B-spline basis functions of degrees p and q in the parametric coordinates ξ and η, respectively. The corresponding bivariate B-spline surface is then defined as

$$\mathbf{S}(\xi, \eta) = \sum_{i=1}^{n_\xi} \sum_{j=1}^{n_\eta} B_{i,p}(\xi)\, B_{j,q}(\eta)\, \mathbf{P}_{i,j}, \tag{2}$$

where n_ξ and n_η are the numbers of basis functions in the ξ- and η-directions, respectively, and $\mathbf{P}_{i,j} \in \mathbb{R}^d$ are the surface control points.

3.2. Knot insertion

Knot insertion is a fundamental operation in spline-based modeling that refines the parametrization without altering the geometry of the curve or surface. By inserting additional knots into the

knot vector, the curve or surface gains more control points, thereby enabling finer local control and facilitating tasks such as curve refinement and surface subdivision. Importantly, knot insertion does not change the shape of the geometry; it only modifies its representation by adding control points. This property makes the technique particularly useful in many applications. In this study, it is employed to extract B-spline curves that lie on a B-spline surface, as presented in the following subsection. Further details on the mathematical formulation, algorithms, and applications of knot insertion can be found in Piegl and Tiller (2012) or similar textbooks.

3.3. B-spline curve extraction from a B-spline surface

Herein we present the procedure for extracting a curve from a B-spline surface corresponding to a fixed value $\xi = \xi^*$ or $\eta = \eta^*$ in the parametric domain. This operation is particularly useful in later stages of the methodology, where B-spline surfaces must be related to toolpath generation and finite element mesh construction.

Given a B-spline surface defined in Eq. (2), the extraction of the B-spline curve $\mathbf{C}(\eta, \xi^*)$ is performed through *knot insertion*. In this process, the fixed parametric value $\xi = \xi^*$ is repeatedly inserted into the knot vector of the ξ-direction until it reaches full multiplicity $(p + 1)$. The resulting refinement produces a new set of control points that directly represent the B-spline curve in the η-direction, ensuring an exact extracted curve that preserves the geometry of the original surface for subsequent use.

An example of extracting a curve from a B-spline surface is shown in Figure 2. The B-spline surface is bi-quadratic and constructed from a 7×6 mesh of control points with open uniform knot vectors. The figure shows the control mesh (green lines) and the corresponding control points (blue dots), together with the resulting B-spline surface. The extracted curve at $\xi = 3.5$ is drawn in magenta, its control points are highlighted in red, and its control polygon is indicated with a dark green line.

We note that in this study, each layer of control points in the y–z plane shares the same x-coordinate, and the control points on the B-spline surfaces used in the following sections are fixed in the x-direction, implying that the extracted curves lie in the y–z planes. In the following application, curves with a prescribed physical x-coordinate, x^*, must be extracted. To determine ξ^* and extract the corresponding curve, one solves $S_x(\xi, \eta) = x^*$ for ξ^*, such that $S_x(\xi^*, \eta) = x^*$, where $S_x(\xi, \eta)$ denotes the x-component of the B-spline surface mapping.

4. Design parameterization

In this section we present the geometrical parameterization of the post-tensioned design together with the design variables used in the optimization problem. We begin by defining the geometry of the design, followed by the placement and parameterization of the cables. Throughout the following sections, we designate the longitudinal direction by x, the width by y, and the height by z.

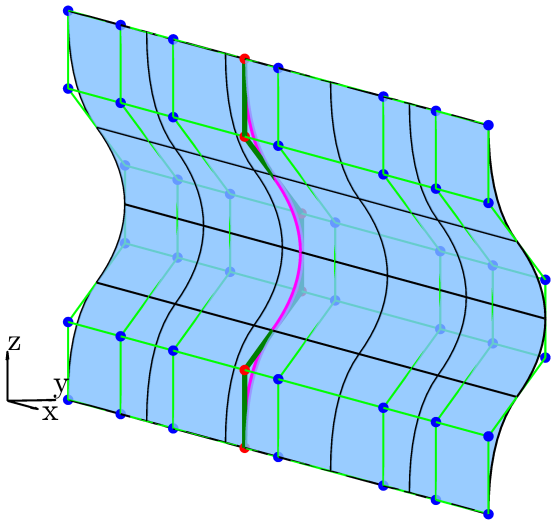

Figure 2: Extraction of a curve from a bi-quadratic B-spline surface. Green lines and blue dots show the control mesh, while the magenta curve with red control points illustrates the extracted B-spline curve.

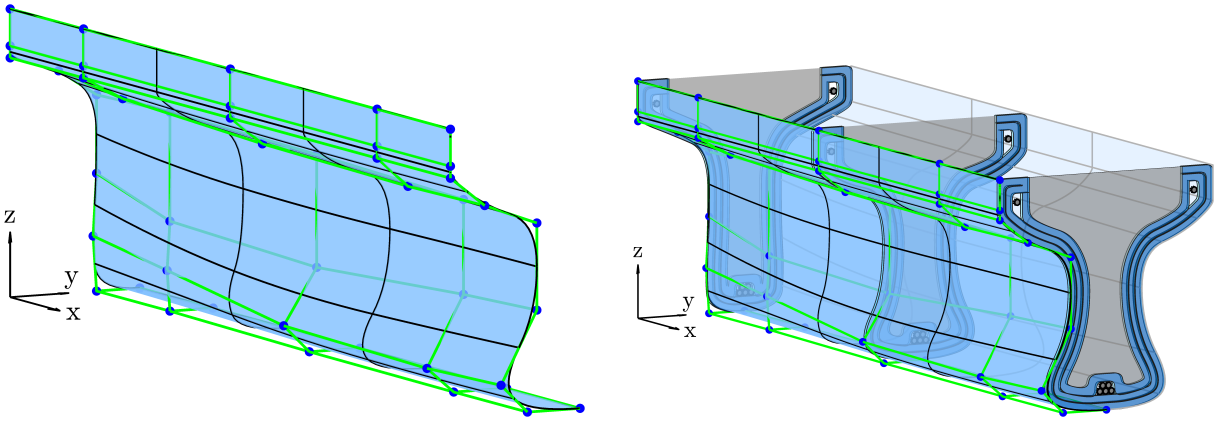

(a) (b)

Figure 3: B-spline surface representations of the outer boundary of a beam. (a) The B-spline surface which parameterizes the symmetric part of the design. (b) Illustration of a complete segment, including cross-sections of the compound cast and 3D-printed design.

4.1. Geometry parameterization

The geometry is defined by a B-spline surface that represents the outer boundary of the design in $\mathbb{R}^3$. From this surface, the 3D-printing toolpath, the cable locations, and the analysis mesh are derived.

The case studies presented in Section 9 include a beam and a unidirectional slab, both exhibiting double symmetry with respect to the mid-length plane and the mid-width plane. Utilizing this symmetry, the B-spline outer surface is defined only over one quarter of the geometry, while the complete design is generated through two successive mirroring operations. This does not limit the generality of the approach, as it is also applicable to geometries without symmetry. An example of the outer surface of a beam design is illustrated in Figure 3a, together with an illustration including cross-sections of the compound cast and 3D-printed design, with the surface mirrored with respect to the mid-width symmetry plane, shown in Figure 3b.

The geometry is modified during optimization by moving the control points of the outer surface within the y–z planes, while their coordinates in the x-direction remain fixed. Moreover, each layer of control points in the cross-sectional direction shares the same longitudinal x-coordinate. We consider the outer surface N_i control points in the longitudinal direction and N_j control points in the cross-sectional direction, where the control points are indexed by i and j accordingly. The N_i-th layer of control points in the longitudinal direction lies on the mid-length symmetry plane. Figures 4a and 4b illustrate the cross-sectional control points for the beam-like and slab-like designs, respectively.

To incorporate additional design requirements, certain control points are restricted from moving within the y–z plane during optimization. Based on the setup defined above, the following restrictions are applied:

1. For each cross-sectional layer i:

   (a) We impose the condition $P^z_{i,1} = P^z_{i,2}$ to ensure a smooth transition across the mid-width symmetry plane, where the superscript denotes the coordinate direction. These two coordinates can therefore be collapsed into a single design variable in the optimization process.

   (b) The control point $\mathbf{P}_{i,1}$ is allowed to move only in the z-direction, while its y-coordinate is fixed. This ensures that $\mathbf{P}_{i,1}$ remains on the mid-width symmetry plane.

   (c) The three upper control points $\mathbf{P}_{i,N_j-2}$ to $\mathbf{P}_{i,N_j}$ remain fixed in order to maintain the width of the design at its upper part and to ensure sufficient depth for accommodating cables, if needed.

2. To ensure a smooth transition across the mid-length symmetry plane, the y- and z-coordinates of the control points in layer $N_i - 1$ are set equal to those of the corresponding control points in layer N_i:

$$P^{(y,z)}_{N_i-1,\,j} = P^{(y,z)}_{N_i,\,j}, \qquad j = 1, \ldots, N_j. \tag{3}$$

3. For the slab design only, the control points are restricted from moving in the y-direction, leaving the z-direction as the sole design variable during optimization. This is more suitable for the typical proportions of slab geometries, which generally have a much larger width compared to their depth, in contrast to beam designs.

4.2. Post-tensioning cable layout

The cables are modeled as B-spline curves whose control points are positioned according to the outer surface geometry, with no independent design variables. As described in Section 2,

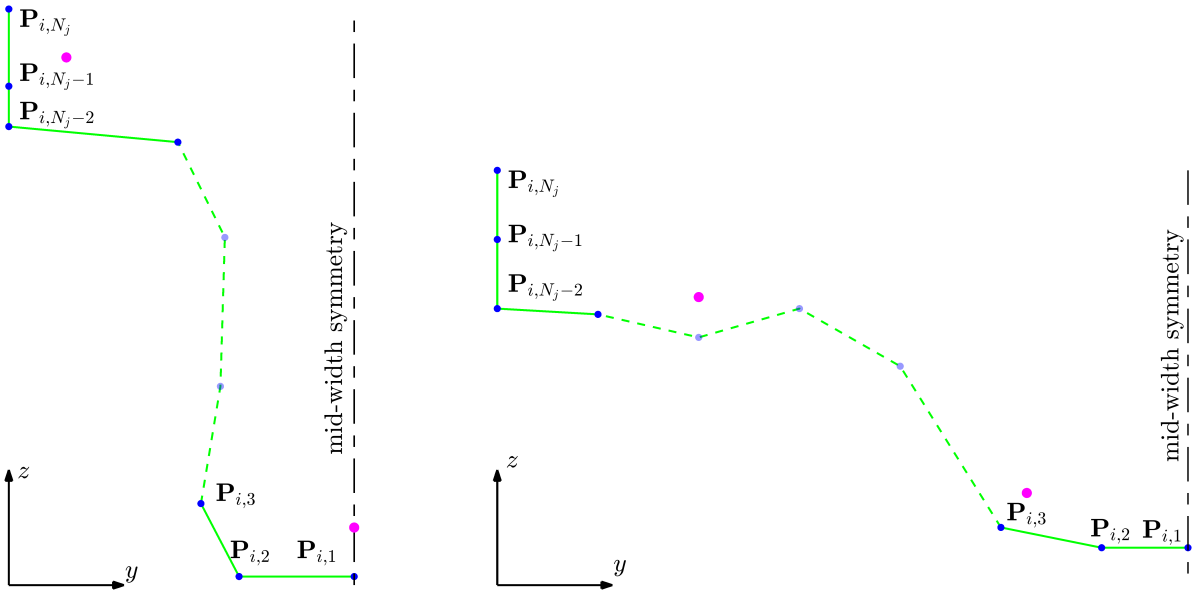

(a) Beam cross-section.

(b) Slab cross-section.

Figure 4: Cross-sectional control points of the outer surface in the y–z plane for (a) the beam and (b) the slab.

the cables are placed inside a cavity located two toolpaths inward from the outer boundary. Accordingly, their positions are prescribed at offsets that account for the width of these layers as well as the required clearance for cable insertion. In the following, we present the cable setup for both the beam and slab designs.

4.2.1. Cable setup: beam design

For the beam case, two groups of prestressing cables are used: an upper group and a lower group. The upper group consists of two cables placed symmetrically about the mid-width of the design, while the lower group forms a concentrated bundle located along the mid-width. While the lower cables primarily serve to reduce displacements and stresses under applied loads, the inclusion of upper cables is motivated by practical considerations. First, the upper cables facilitate the assembly of the 3D-printed segments. Second, they help introduce compressive forces between layers, which is beneficial given the relatively low tensile capacity between printed layers.

The upper cables are located at prescribed horizontal and vertical offsets from the upper corners of the cross-section. Since these corners remain unchanged during optimization, the positions of the upper cables remain fixed. In contrast, the lower cables are positioned at the mid-width of the beam and at a fixed vertical offset from the bottom surface. To represent this group, a B-spline curve is constructed whose control points are positioned according to the bottom control points of the outer surface. These control points are assigned elevated z-coordinates corresponding to the prescribed cable offset, while their (x, y)-coordinates remain aligned with the bottom control points of the outer surface. Thus, the set of cable control points is

$$P_{\text{cables},\,i} = \left(P^x_{i,1},\ P^y_{i,1},\ P^z_{i,1} + d_{\text{cable}}\right), \qquad i = 1, \ldots, N_i,$$

where d_{cable} is the vertical offset from the bottom control points of the outer surface. Since these control points move during the optimization, the positions of the lower cables are updated accordingly. The locations of the control points representing the cables are illustrated by the magenta circles in Figure 4a.

4.2.2. Cable setup: slab design

For the slab case, four cable groups are used in the full model, of which only two appear in the quarter-symmetric domain. Both groups are attached to the evolving outer surface, so their positions are updated consistently during the optimization as the slab's outer geometry changes.

Unlike the beam case, attaching the cables to a predefined line of control points does not guarantee that they remain at a prescribed physical distance from the outer surface. Therefore, the cable groups are distributed evenly along the width of the slab and are associated with prescribed values of the cross-sectional parametric coordinate of the outer surface. Assuming that control point i of a cable is attached to a parametric location (ξ_i^*, η_i^*) on the outer surface, the corresponding cable control point is placed by offsetting this surface point in the normal direction:

$$P_{\text{cable},\,i} = S(\xi_i^*, \eta_i^*) + \mathbf{n}(\xi_i^*, \eta_i^*)\, d_{\text{cable}},$$

where $S(\xi_i^*, \eta_i^*)$ is the point on the outer surface, $\mathbf{n}(\xi_i^*, \eta_i^*)$ is the outward unit normal at that point, and d_{cable} is the prescribed physical cable offset. Here, ξ_i^* corresponds to the longitudinal (x-) direction and η_i^* to the cross-sectional direction. The values of ξ_i^* are chosen such that the x-coordinates of the cable control points coincide with those of the outer surface, while the values of η_i^* are selected so that the cables are evenly distributed across the slab width.

5. Toolpath generation

In this section we describe the procedure for toolpath generation and present an approach for approximating its length, for later use in the optimization framework.

5.1. Procedure for toolpath generation

The toolpath generation for the printed component is performed using a staged procedure that constructs three inward offsets of the outer geometry and incorporates cavities for cable insertion. The process begins by extracting the curves corresponding to the 3D-printed layers on the outer surface, which represents a quarter-symmetric portion of the model. After applying the required offsets and geometric modifications to introduce the cable cavities, the resulting toolpath is mirrored to obtain the full-layer geometry.

We demonstrate this procedure using Figure 5 for a beam design. The toolpath height and width are assumed to be l_h and l_w, respectively, with an overlap of approximately l_o between adjacent toolpaths, as clarified in Section 2. The following steps are performed:

1. Determine the x-coordinates of the layers. The layers are positioned sequentially along the x-direction with a spacing of $l_h - l_0$ between consecutive layers.

2. For each layer, following Section 3.3, extract the curve on the outer surface corresponding to its x-coordinate. The extracted curve is highlighted in blue in Figure 5.

3. Generate three inward offsets of the extracted curve, located at:

   - $l_w/2$ (centerline of the outer toolpath),
   - $l_w/2 + (l_w - l_0)$ (centerline of the middle toolpath),
   - $l_w/2 + 2(l_w - l_0)$ (centerline of the inner toolpath).

   This step is illustrated in Figure 5a.

4. Apply the required geometric modifications to introduce the cable cavities and to connect the toolpaths in a non-overlapping manner. The modifications include:

   (a) Creating cavities between the middle and the innermost toolpaths to accommodate cables.

   (b) Modifying the offsets at their endpoints to obtain well-shaped toolpaths, as shown in Figure 5b.

5. Mirror the resulting toolpaths to obtain the full cross-section of the layer (Figure 5c).

6. Connect the mirrored segments to obtain the continuous toolpath for the layer (Figure 5d). This step ensures that the endpoints of all offset curves are joined smoothly.

The resulting centerline toolpath is shown in Figure 5e.

5.2. Toolpath length

Several quantities in the optimization framework depend on the toolpath length of each layer and on its derivatives with respect to the shape design variables. Because direct differentiation of the toolpath generation procedure is challenging, we adopt a linear approximation of the layer length. The input for the linear approximation is the length of the control polygon of the corresponding B-spline curve extracted from the outer surface, as described in Section 3.3. This linear approximation is constructed as follows:

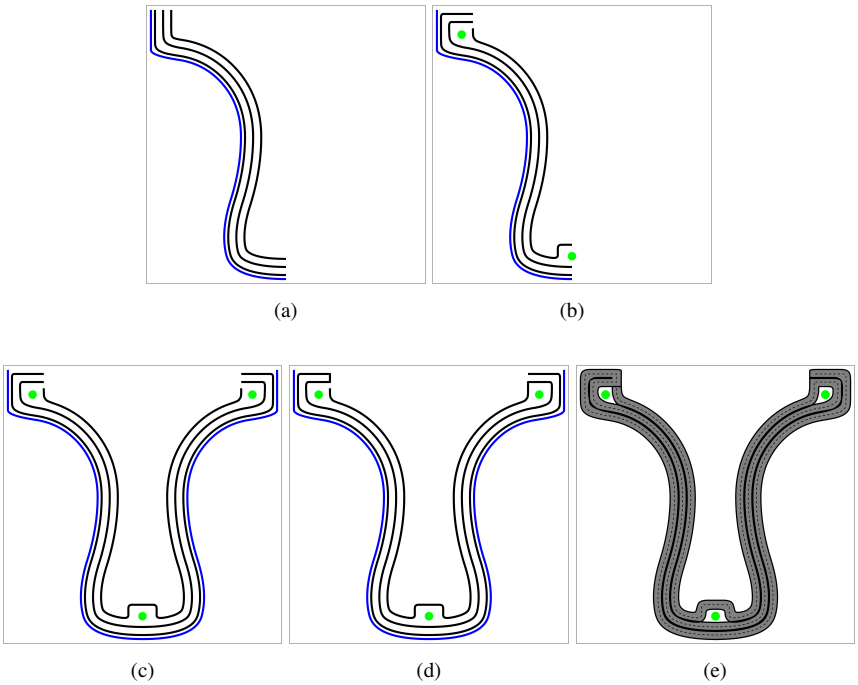

Figure 5: Toolpath generation steps for a beam design.

1. Generate an outer-surface geometry, either by randomly perturbing the design variables (the surface control points) or by using actual designs obtained from optimizations in which the toolpath length is not yet required.

2. Extract the curves on the outer surface corresponding to the 3D-printed layers, following Section 3.3.

3. Compute the lengths of the outer control polygons of the extracted curves and store them in a vector denoted by $\mathbf{L}_P$.

4. Generate the toolpath for each layer according to Section 5.1 and compute the actual toolpath lengths in all layers, storing them in a vector denoted by $\mathbf{L}_L$.

5. Fit a linear relation between $\mathbf{L}_L$ and $\mathbf{L}_P$. For each layer i, the approximation takes the form

$$L_{Li} \approx a \cdot L_{Pi} + b\,, \tag{4}$$

   where a and b are fitting parameters.

Since the polygon length L_{Pi} is directly linked to the design variables through a fully differentiable procedure, this approximation provides a simple and differentiable connection between the toolpath length L_{Li} and the shape variables $\mathbf{X}$. In the Examples section, we demonstrate that the linear relationship provides an adequate approximation of the actual variation of the toolpath length.

6. Governing equations

In this section, we present the governing equations that define the physical problem addressed in this study, along with their numerical solution. The concrete is modeled as a continuum of linear elastic material, analyzed using the finite element method and subjected to various types of loading. The following subsections first describe the construction of the finite element model and then detail the applied loads and their computation.

6.1. Finite element model

The finite element model used in this study does not distinguish between the printed and cast concrete. Both parts are treated as a single homogeneous material, assuming that similar material properties can be achieved in both phases. Since the outer geometry of the design is represented by a B-spline surface, concrete material occupies the interior region enclosed by the surface while the exterior regions are treated as void.

To construct the finite element model, we embed the surface within a structured finite element mesh that covers the design domain and adopt a density-based approach to differentiate between material and void regions. According to this approach, a pseudo-density parameter ρ is assigned to each finite element, ranging between 0 and 1, where $\rho = 0$ represents void and $\rho = 1$ represents material. The elasticity modulus of each element is then computed through a linear relation to the density parameter:

$$E_i(\rho_i) = E_{\min} + \rho_i \left(E_{\max} - E_{\min}\right), \tag{5}$$

where $E_{\max}$ denotes the elastic modulus of concrete and $E_{\min}$ is a small positive value introduced to avoid elements with zero stiffness. Without loss of generality, this study employs uniform solid eight-node hexahedral (brick) elements.

The density parameter for each finite element is determined according to a signed distance function of the B-spline surface in the cross-sectional y–z plane. For elements whose centroids have a positive distance (i.e., located inside the defined interior), the densities are driven toward $\rho = 1$, while for elements with negative distance (i.e., outside the surface), the densities are driven toward $\rho = 0$. Elements located near the boundary of the surface are assigned intermediate values, smoothly interpolating between 0 and 1.

The signed distance between an element and the surface in the cross-sectional plane is computed as follows. First, for each slice of elements in the y–z plane, the outer curve of the surface is extracted according to Section 3.3 at $x = x_c$, where x_c denotes the longitudinal coordinate of the element centroids in that plane. Then, for each element i in this slice, the signed distance is evaluated with respect to the extracted curve, which is represented as a parametric quadratic B-spline:

$$\xi^* = \arg\min_{\xi} \left\| \mathbf{x}_i - \mathbf{C}(\xi) \right\|, \tag{6}$$

$$d_i = \operatorname{sign}\Big(\big(\mathbf{x}_i - \mathbf{C}(\xi^*) \big) \cdot \mathbf{n}(\xi^*) \Big) \left\| \mathbf{x}_i - \mathbf{C}(\xi^*) \right\|, \tag{7}$$

where ξ^* is the parameter value that minimizes the distance, $\mathbf{x}_i$ is the centroid of element i, and $\mathbf{n}(\xi^*)$ is the unit normal to the curve at the point $\mathbf{C}(\xi^*)$.

For the quadratic B-spline surfaces and curves employed in this work, the signed distance can be computed analytically. This is achieved by evaluating the distances with respect to each Bézier segment of the curve and selecting the segment that yields the minimal value. Equations (7) and (6) are not smooth for elements whose sign (i.e., relative side with respect to the curve) changes, or for elements whose closest point switches between Bézier segments. Nevertheless, for sufficiently small perturbations—where the sign remains unchanged and the closest point continues to lie on the same Bézier segment—the mapping is differentiable. This is the case considered in the sensitivity analysis in Section 8. Moreover, this lack of global smoothness has not shown a noticeable effect on the convergence of the optimization, and smooth optimization behavior is observed in the examples presented in Section 9.

After computing the signed distances, the element densities are obtained using a smooth projection filter:

$$\rho_i \;=\; \frac{1}{1 + \exp\big(-\beta d_i \big)}, \tag{8}$$

where ρ_i denotes the resulting density of element i, d_i is the signed y–z planar distance of its centroid, and β is a sharpness parameter that controls the smoothness of the transition between void and solid regions.

The parameter β is selected in accordance with the resolution of the finite element discretization such that $\rho = 0.95$ at a signed distance equal to the finite element side length e_{size}, and $\rho = 0.05$ at a signed distance of $-e_{\text{size}}$. Accordingly,

$$\beta \;=\; -\frac{\ln\left(\frac{1-0.95}{0.95}\right)}{e_{\text{size}}}. \tag{9}$$

Figure 6 illustrates the relation between density and signed distance. In this example, assuming an element size of $e_{\text{size}} = 0.025\,\text{m}$ (consistent with the discretization used in the numerical examples), the corresponding value of the sharpness parameter is $\beta = 117.77$. An illustration of a slice of finite elements in the y–z plane, showing the density distribution, is presented in Figure 7. In this figure, black corresponds to $\rho = 1$ (solid) and white corresponds to $\rho = 0$ (void), with a smooth density transition near the boundary. The outer curve is represented in blue.

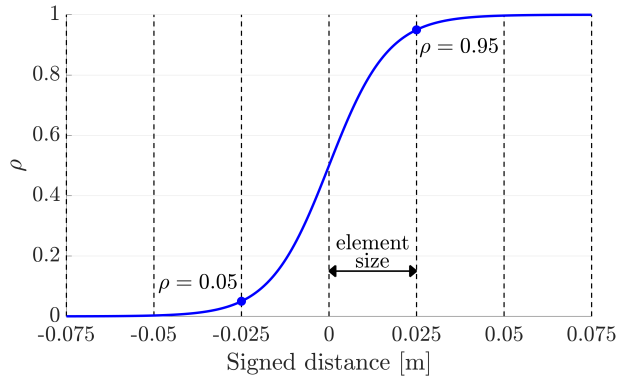

Figure 6: Relation between the signed distance d and the resulting density ρ, based on the smooth projection filter.

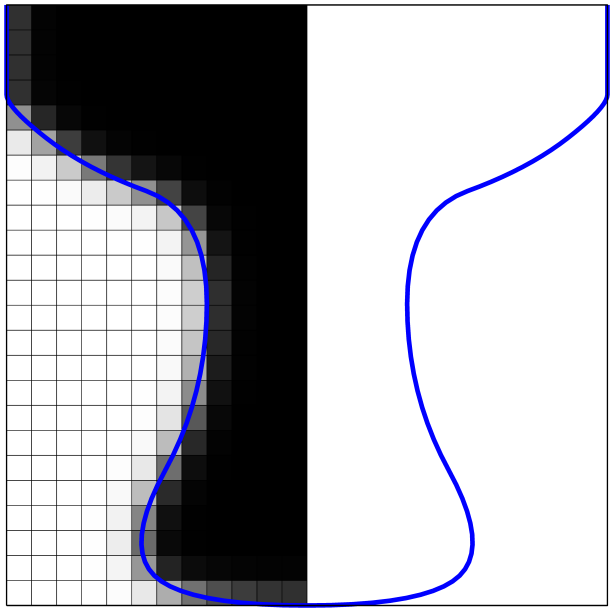

Figure 7: A slice of finite elements in the y–z plane together with their density distribution. Black indicates $\rho = 1$ (solid) and white indicates $\rho = 0$ (void), with a smooth density transition near the boundary curve shown in blue. The cross-section is symmetric about the mid-width axis, where only half of the symmetric part needs to be modeled.

6.2. Applied loads

The post-tensioned members in this study are subjected to four types of forces: (i) $\mathbf{f}_l$, live load; (ii) $\mathbf{f}_d$, dead load; (iii) $\mathbf{f}_s$, self-weight; (iv) $\mathbf{f}_p$, prestressing force.

Dead and live loads are applied to the structural elements in specified regions according to the problem settings. The self-weight is evaluated from the density layout, with the weight of each finite element distributed to its associated degrees of freedom. For a finite element i, the local nodal force vector due to self-weight is given by

$$\mathbf{f}_{s,i} = \gamma_c \, v_i \, \rho_i \, \mathbf{N}_i,$$

where γ_c is the specific weight of concrete, v_i is the volume of element i, ρ_i is its density parameter, and $\mathbf{N}_i$ denotes the shape functions of the element.

The prestressing forces are incorporated into the finite element model following the procedure presented by Shakur et al. (2024). The action of a post-tensioning cable is represented by two contributions: distributed forces along the cable arising from its curvature, and concentrated forces at the anchorages. These contributions are transferred to the finite element nodes through the element basis functions, resulting in the nodal prestressing force vector $\mathbf{f}_p$. Complete details on the evaluation of the prestressing forces, including full derivations and illustrative figures, are provided in Shakur et al. (2024). For completeness, the computational steps for evaluating $\mathbf{f}_p$ can be summarized as follows:

1. Cable–mesh intersections: The intersections of the cable with the finite element mesh are determined analytically by solving quadratic equations, similar to the case of Eqs. (6) and (7).

2. Curvature-induced forces: For each cable segment between two intersection points, a distributed load proportional to the cable force and the local curvature is defined in the normal direction of the cable.

3. Projection to nodes: Each distributed load segment, lying entirely within the domain of a single finite element, is projected onto the nodes of that element through integration over the cable shape using the element shape functions.

4. Anchorage forces: At the cable ends, concentrated forces equal to the cable force and oriented tangentially to the cable are applied.

5. Assembly: The nodal force contributions from curvature and anchorage effects are assembled into the global prestressing force vector,

$$\mathbf{f}_p = \sum_{i=1}^{N_\mathrm{E}} \left(\mathbf{f}_{p,i}^{\mathrm{Curv}} + \mathbf{f}_{p,i}^{\mathrm{Anc}} \right), \tag{10}$$

   where N_E denotes the total number of finite elements in the mesh. Here, $\mathbf{f}_{p,i}^{\mathrm{Curv}}$ represents the nodal force contribution due to curvature-induced loads, and $\mathbf{f}_{p,i}^{\mathrm{Anc}}$ corresponds to the contribution from anchorage forces. For elements not intersected by the cable, both $\mathbf{f}_{p,i}^{\mathrm{Curv}}$ and $\mathbf{f}_{p,i}^{\mathrm{Anc}}$ vanish.

For clarity in the subsequent sections, the displacements associated with the force vectors $\mathbf{f}_p$, $\mathbf{f}_s$, $\mathbf{f}_d$, and $\mathbf{f}_l$ are denoted by $\mathbf{u}_p$, $\mathbf{u}_s$, $\mathbf{u}_d$, and $\mathbf{u}_l$, respectively. When multiple forces act simultaneously, their corresponding displacements are indicated by concatenated subscripts. For example, $\mathbf{u}_{sd}$ denotes the displacement response to $\mathbf{f}_s + \mathbf{f}_d$, while $\mathbf{u}_{sdp}$ refers to the displacement produced by $\mathbf{f}_s + \mathbf{f}_d + \mathbf{f}_p$. Each displacement vector $\mathbf{u}_{(\cdot)}$ is computed by solving the governing

equation $\mathbf{K}\mathbf{u}_{(\cdot)} = \mathbf{f}_{(\cdot)}$, with $\mathbf{K}$ denoting the stiffness matrix of the linear-elastic concrete domain, assembled from the element-wise values of Eq. (5).

In this study, the stiffness of the cable and force losses along its length are neglected, as their impact on the optimized design is assumed to be small. Nevertheless, the formulation can readily incorporate immediate losses arising from friction, anchorage slip, and elastic shortening, as these effects depend explicitly on the prestressing force and cable curvature. Additionally, long-term effects such as creep, shrinkage, and relaxation may be evaluated from the cable forces and the concrete response, and subsequently incorporated into the computation of the prestressing forces.

7. Problem formulation

In this section, we present the formulation of the optimization problem, including details of the objective function and the associated constraints. Each of these components is first discussed separately in the following subsections. Afterwards, they are combined to provide the complete problem formulation. The optimization incorporates three types of design variables:

(i) Shape design variables, denoted by $\mathbf{X}$. These represent the outer surface of the structure, as described in Section 4.

(ii) Prestressing forces, denoted by $\mathbf{T}$. In this study, each group of cables is assigned a design variable representing its prestressing force, which counteracts the applied loads, as discussed in Section 7.1.1.

(iii) Printing speed, denoted by v. While a high printing speed improves fabrication efficiency, excessively large speeds may lead to unbuildable designs (see Section 7.3). To balance efficiency and buildability, the objective to be minimized includes printing time, and the printing speed is therefore included as a design variable that is assumed constant throughout the fabrication process.

These variables are collectively represented in the design vector

$$\tilde{\mathbf{X}} = [\, \mathbf{X},\, \mathbf{T},\, v \,].$$

7.1. Objective function

The objective of the optimization involves multiple physical measures to account for different design and fabrication considerations, including the minimization of displacement-related terms, compliance, prestressing force, and printing time. In the following, we provide further details on the motivation for incorporating these components and present their formulations.

7.1.1. Displacement minimization

In prestressed concrete design, a common practice is to select the prestressing forces such that they balance a portion of the permanent loads acting on the structure. The specific response measure to be balanced (e.g., displacements or stresses) may be chosen according to the design intent. In this work, we require the prestressing forces $\mathbf{f}_p$ to counteract the absolute displacement in the upper chord of the beam caused by the self-weight $\mathbf{f}_s$ and a fraction of the permanent load, denoted as

$$\mathbf{f}_{\tilde{d}} = w_d \, \mathbf{f}_d, \tag{11}$$

where $w_d \in [0, 1]$ is the dead-load factor. The corresponding balancing measure is expressed as

$$\phi_1 = (\mathbf{l} \circ \mathbf{u}_{sp\tilde{d}})^T (\mathbf{l} \circ \mathbf{u}_{sp\tilde{d}}), \tag{12}$$

where $\mathbf{l}$ identifies the degrees of freedom at which displacements are to be balanced (namely, the vertical DOFs on the top surface of the structure), and $\circ$ denotes component-wise multiplication. This term was originally developed and explored by Amir and Shakour (2018).

7.1.2. Compliance minimization

The second part of the objective aims to minimize the compliance due to the remaining portion of the dead load, $\mathbf{f}_{\tilde{\tilde{d}}} = (1 - w_d) \, \mathbf{f}_d$, and the live load $\mathbf{f}_l$:

$$\phi_2 = \mathbf{f}^T_{\tilde{\tilde{d}}l} \mathbf{u}_{\tilde{\tilde{d}}l}. \tag{13}$$

The key difference between ϕ_1 and ϕ_2 is that ϕ_2 drives the concrete geometry towards the stiffest design under the selected loads, whereas ϕ_1 is not directly related to stiffness. Minimizing only ϕ_1 could lead to a neutral displacement field in the selected region, even if certain parts of the structure are less stiff. Since this outcome is undesirable, the stiffness-related measure ϕ_2 is necessary.

7.1.3. Prestressing force minimization

Previous studies have shown that when the prestressing force is excessively large, the topology may adapt by softening parts of the structure in order to reach neutral displacements (Amir and Shakour, 2018). To mitigate this effect, we additionally minimize the prestressing forces in the cable groups located in the bottom parts of the members:

$$\phi_3 = \mathbf{T}_b, \tag{14}$$

where $\mathbf{T}_b$ denotes the vector containing the prestressing force assigned to each group of prestressing cables.

7.1.4. Printing time minimization

To enhance fabrication efficiency, we incorporate a printing time minimization term. The printed toolpath length can reach several thousand meters, and even small increases in printing speed can significantly reduce the total fabrication time. The printing time is represented by

$$\phi_4 = \frac{L_T}{v}, \tag{15}$$

where L_T denotes the total length of the printing toolpath, evaluated as described in Section 5, and v is the printing speed.

7.1.5. Total objective

Considering all four measures to be minimized, the final objective is scaled and formulated as

$$\tilde{\phi} = w_1 \frac{\phi_1}{\phi_1^0} + w_2 \frac{\phi_2}{\phi_2^0} + w_3 \frac{\phi_3}{\phi_3^0} + w_4 \frac{\phi_4}{\phi_4^0}, \tag{16}$$

where w_1, w_2, w_3, and w_4 are weighting coefficients, and ϕ_1^0, ϕ_2^0, ϕ_3^0, and ϕ_4^0 are the initial values of each measure used for scaling.

7.2. Volume constraint

The volume constraint is formulated based on the density field over the mesh used for the finite element analysis, as presented in Section 6. The total volume V is computed as

$$V(\mathbf{X}) = \sum_{i=1}^{N_\mathrm{E}} \rho_i(\mathbf{X})\, v_i, \tag{17}$$

where N_E is the total number of finite elements, v_i is the volume of element i, and $\rho_i(\mathbf{X})$ is the density value of element i as a function of the shape design variables $\mathbf{X}$, computed using Eq. (8). The corresponding volume constraint is then expressed as

$$V(\mathbf{X}) \leq V^*, \tag{18}$$

where V^* denotes the prescribed upper bound on the allowable volume.

7.3. Buildability constraint

In this paper, *buildability* refers to the ability of a generated geometry to be printed without collapsing under its own weight during the printing process. Concrete exhibits a relatively slow stiffening rate compared to the printing rate, and each freshly deposited layer possesses only a fraction of its final mechanical strength. The design must therefore ensure that during printing, the structure can safely support its self-weight without significantly deforming, while accounting for the evolving material strength. This check is carried out by comparing the time-dependent

static yield strength of the material with the shear stresses induced by the self-weight of the subsequently deposited layer at different points in time.

For formulating the buildability constraint, we extend the approach of Mogra (2023), which is limited to circular layer geometries, by generalizing the method to layers of arbitrary shape. To evaluate the static yield strength during printing, we use the time-dependent model of Kruger et al. (2019), which assumes an initial strength at deposition that increases gradually over time. The yield strength evolves according to a piecewise linear function that accounts for the changing hardening rates of fresh concrete. The function parameters depend on the concrete mix and can be adjusted using fibers or chemical accelerators. Appendix A provides the parameters for the four different concrete mixtures considered in this paper, each with a different fiber content, based on the results of the research reported by (Asaf et al., 2024b).

To ensure buildability, a shear stress check is carried out at the completion of each printed layer to verify that none of the previously deposited layers exceed their available shear capacity. Let Layer_j denote the jth 3D-printed layer. When Layer_j is completed at time T_j, the verification procedure is applied to that layer and to all previously printed layers $\text{Layer}_1, \ldots, \text{Layer}_j$, to confirm that each can sustain its self-weight as well as the weight of the layers deposited above it.

The verification scheme is illustrated in Table 1. In the table, $W_{i:j}$ denotes the cumulative self-weight of layers from Layer_i to Layer_j, i.e., $W_{i:j} = \sum_{k=i}^{j} w_k$ (e.g., $W_{1:2} = w_1 + w_2$, $W_{2:3} = w_2 + w_3$), where w_k is the self-weight of Layer_k. Similarly, the term ΔT_{ij} denotes the elapsed time between the deposition of Layer_i and the verification at time T_j, i.e., $\Delta T_{ij} = T_j - T_i$. Equivalently, ΔT_{ij} can be evaluated as the accumulated printing time of the layers between i and j, $\Delta T_{ij} = \sum_{k=i+1}^{j} t_k$ (e.g., $\Delta T_{i:i} = 0$ and $\Delta T_{1:3} = t_2 + t_3$), where t_k is the printing time of Layer_k. Finally, τ_{ij} denotes the evaluated shear stress in Layer_i at the verification time associated with Layer_j, computed following Kruger et al. (2019) as

$$\tau_{ij} = \frac{W_{i:j}}{2 f_{AR} A_i}, \tag{19}$$

where A_i is the cross-sectional area of Layer_i and f_{AR} is a correction factor that depends on the geometry of the cross-section of the printed toolpath. The corresponding yield strength of Layer_i at the verification time associated with Layer_j is denoted by $\tilde{\tau}_{ij}$. In this scheme, each Layer_i is checked at every time T_j for all $j \geq i$. For a segment consisting of N_l layers, the total number of verification checks is

$$N_{\text{checks}} = \frac{N_l(N_l + 1)}{2}, \tag{20}$$

and this number is multiplied by the number of segments if the design is divided into multiple 3D-printed segments.

	T_1	T_2	T_3	T_j
Layer_1	$\tau(W_{1:1}) \leq \tilde{\tau}(\Delta T_{11})$	$\tau(W_{1:2}) \leq \tilde{\tau}(\Delta T_{12})$	$\tau(W_{1:3}) \leq \tilde{\tau}(\Delta T_{13})$	$\tau(W_{1:j}) \leq \tilde{\tau}(\Delta T_{1j})$
Layer_2	–	$\tau(W_{2:2}) \leq \tilde{\tau}(\Delta T_{22})$	$\tau(W_{2:3}) \leq \tilde{\tau}(\Delta T_{23})$	$\tau(W_{2:j}) \leq \tilde{\tau}(\Delta T_{2j})$
Layer_3	–	–	$\tau(W_{3:3}) \leq \tilde{\tau}(\Delta T_{33})$	$\tau(W_{3:j}) \leq \tilde{\tau}(\Delta T_{3j})$
Layer_i	–	–	–	$\tau(W_{i:j}) \leq \tilde{\tau}(\Delta T_{ij})$

Table 1: Verification scheme at different points in time. Rows represent the checked printed layer Layer_i, and columns indicate the corresponding verification times T_j. The subscripts i and j are omitted from τ and $\tilde{\tau}$ for brevity.

To proceed with the formulation of the buildability constraint, we need the length of each 3D-printed layer. Assuming the layer lies at $x = x_l$, we first extract its corresponding curve on the outer surface, denoted by C_l, according to Section 3.3. We then adopt the expression in Eq. (4), which relates the length of the outer polygon of the extracted curve to the length of the layer. Once the layer length is known, other required measures such as area, volume, and weight can be derived accordingly.

By organizing the x-coordinates of each layer into a vector $\mathbf{x}_l$, and given the outer surface, the toolpath width l_w and height l_h, the parameters a and b from Eq. (4), the printing speed v, the concrete specific weight γ_c, and the number of layers N_l, Algorithm 1 computes the vectors $\mathbf{L}$, $\mathbf{A}$, $\mathbf{w}$, and $\mathbf{t}$, which store the length, area, weight, and printing time of each layer, respectively. Subsequently, the ratio $\tau_{ij}/\tilde{\tau}_{ij}$ is evaluated for all verification points and the results are collected in the matrix $\mathbf{R}$ following the procedure outlined in Algorithm 2.

Algorithm 1 Computation of Geometric and Physical Quantities of the Layers

Input: OuterSurface, $\mathbf{x}_l$, l_w, l_h, a, b, v, γ_c, N_l
Output: $\mathbf{L}$, $\mathbf{A}$, $\mathbf{w}$, $\mathbf{t}$

for each layer $i = 1$ to N_l **do**
    Extract curve C_l at $x = x_{l,i}$ (Section 3.3)
    Compute L_{Pi}, the length of the outer polygon of C_l
    Compute layer length: $L_{Li} = a \cdot L_{Pi} + b$ (Eq. (4))
    Compute cross-sectional area: $A_i = L_{Li} \cdot l_w$
    Compute layer weight: $w_i = A_i \cdot l_h \cdot \gamma_c$
    Compute printing time: $t_i = \frac{L_{Li}}{v}$
end for

By the nature of the problem, the matrix $\mathbf{R}$ is upper triangular: each column corresponds to the time at which a layer Layer_j is completed, while each row corresponds to the layers that must be checked at that time. To ensure a buildable design, all ratios in $\mathbf{R}$ must be less than 1. Accordingly, to consolidate all checks into a single constraint, we approximate the maximal ratio via the p-norm. Some designs, however, may not be printable in a single run due to printer limitations or practical considerations such as transportation, and may therefore be segmented into multiple 3D-printed parts. In light of this, the inclusive buildability constraint is formulated as follows:

Algorithm 2 Computation of Stress Ratio Matrix **R** for Buildability

Input: **L**, **A**, **w**, **t**
Output: **R**

for each printed layer $j = 1$ to N_l **do**
  for each underlying layer $i = 1$ to j **do**
  / computing actual and allowable stresses in layer i at time T_j */*
    Compute shear stress: $\tau_{ij} = \frac{W_{i:j}}{2 f_{AR} A_i} = \frac{\sum_{k=i}^{j} w_k}{2 f_{AR} A_i}$
    Compute the time difference between layers i and j: $\Delta T_{ij} = \sum_{k=i+1}^{j} t_k$
    Compute allowable shear strength: $\tilde{\tau_{ij}}(\Delta T_{i:j})$
    Compute stress ratio: $R_{ij} = \frac{\tau_{ij}}{\tilde{\tau}_{ij}}$
  end for
end for

$$R^{\text{seg}}_{\text{max-}p\text{norm}} = \left(\sum_{k=1}^{N_{\text{seg}}} \sum_{j=1}^{N_l^{(k)}} \sum_{i=1}^{j} \left(R_{ij}^{(k)} \right)^{p_b} \right)^{\frac{1}{p_b}}, \tag{21}$$

where p_b is the sharpness parameter in the p-norm formulation, N_{seg} is the total number of segments, $N_l^{(k)}$ is the number of layers in segment k, and $R_{ij}^{(k)}$ denotes the stress ratio corresponding to layer i at time t_j within segment k. The corresponding constraint is then expressed as

$$R^{\text{seg}}_{\text{max-}p\text{norm}} \leq \tilde{R}^*, \tag{22}$$

where $\tilde{R}^*$ is the maximal allowed ratio imposed in the optimization. Since the maximal allowable ratio should naturally be restricted to $R^* = 1$ to ensure buildability, the parameter $\tilde{R}^*$ is introduced to enforce the prescribed maximal ratio R^* while avoiding overestimation caused by the p-norm approximation. To achieve this, $\tilde{R}^*$ is updated periodically during the optimization process with respect to the actual maximal ratio $R_{\text{Actual\_Max}}$, as

$$\tilde{R}^* = R^* \frac{R^{\text{seg}}_{\text{max-}p\text{norm}}}{R_{\text{Actual\_Max}}}. \tag{23}$$

7.4. Geometric regularization constraints

To promote more regularized geometries of the 3D-printed design in the optimization process, additional geometric constraints are imposed on the outer surface. Specifically, we impose lower bounds on (i) the minimal distance between consecutive control points and (ii) the minimal angle formed by consecutive control-polygon segments. These constraints ensure that the geometry remains well-conditioned, preventing sharp angles or overly concentrated control points, both of which may lead to numerical instabilities or impractical printing paths. A generic control polygon is shown in Figure 8 to illustrate these constraints.

The constraints are applied to the distances and angles of the polygon in the cross-sectional

direction, whose control points are indexed by j in the figure. Hence, for each control polygon in the longitudinal direction i^*, the constraints are formulated on the set of control points $\{\mathbf{P}_{i^*,j}\}_{j=1}^{N_j}$.

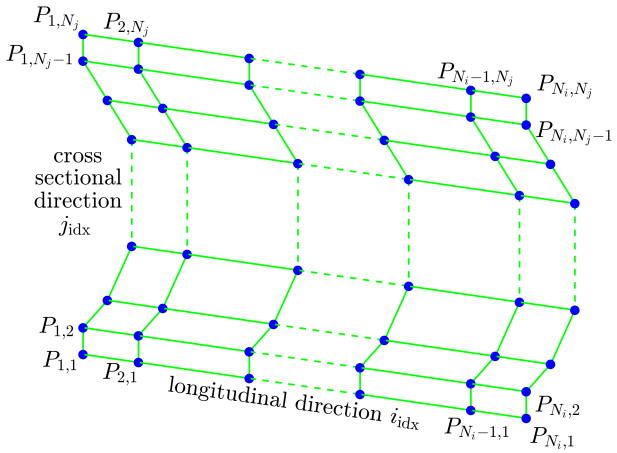

Figure 8: A generic control polygon representing the outer surface, with its control points denoted by $\mathbf{P}_{i,j}$. The mesh consists of $N_i \times N_j$ control points, where N_i and N_j represent the number of control points in the longitudinal and cross-sectional directions, respectively.

7.4.1. Minimal distance constraint

A lower bound is imposed on the minimal distance between consecutive control points in the cross-sectional direction. Following Figure 8, these distances are computed as

$$d_{ij} = \|\mathbf{P}_{i,j+1} - \mathbf{P}_{i,j}\|, \tag{24}$$

for $i = 1, \ldots, N_i$ and $j = 1, \ldots, N_j - 1$. Imposing a minimum distance constraint is achieved using a p-norm approximation:

$$d_{\text{min-}p\text{norm}} = \left(\sum_{i=1}^{N_i} \sum_{j=1}^{N_j-1} d_{ij}^{-p_d} \right)^{-1/p_d}, \tag{25}$$

where p_d is a sharpness parameter that controls the accuracy of the approximation. The corresponding constraint is then written as

$$d_{\text{min-}p\text{norm}} \geq \tilde{d}^*, \tag{26}$$

where $\tilde{d}^*$ is the minimal allowable distance imposed in the optimization. Similar to the buildability constraint, this value is updated during the optimization process to avoid underestimation caused by the p-norm approximation and to capture the true required minimal distance. Denoting the true prescribed minimal allowable distance by d^*, the parameter $\tilde{d}^*$ is evaluated as

$$\tilde{d}^* = d^* \frac{d_{\text{Actual\_Min}}}{d_{\text{min-}p\text{norm}}}, \tag{27}$$

where $d_{\text{Actual\_Min}}$ denotes the actual minimal distance.

7.4.2. Minimal angle constraint

A lower bound is imposed on the minimal interior angle formed by consecutive control-polygon segments in the cross-sectional direction. Following Figure 8, these angles are computed at each interior vertex of the control polygon as

$$\theta_{ij} = \arccos\left(\frac{(\mathbf{P}_{i,j+1} - \mathbf{P}_{i,j}) \cdot (\mathbf{P}_{i,j-1} - \mathbf{P}_{i,j})}{\|\mathbf{P}_{i,j+1} - \mathbf{P}_{i,j}\| \, \|\mathbf{P}_{i,j-1} - \mathbf{P}_{i,j}\|}\right), \tag{28}$$

for $i = 1, \ldots, N_i$ and $j = 2, \ldots, N_j - 1$, where θ_{ij} denotes the angle formed at vertex $\mathbf{P}_{i,j}$. Similar to the minimal distance constraint, the minimum angle is approximated using a p-norm formulation:

$$\theta_{\min\text{-}p\text{norm}} = \left(\sum_{i=1}^{N_i} \sum_{j=2}^{N_j-1} \theta_{ij}^{-p_\theta}\right)^{-\frac{1}{p_\theta}}, \tag{29}$$

where p_θ is a sharpness parameter controlling the accuracy of the approximation. The corresponding constraint is then written as

$$\theta_{\min\text{-}p\text{norm}} \geq \tilde{\theta}^*, \tag{30}$$

where $\tilde{\theta}^*$ is the minimal allowable angle imposed in the optimization. Similar to the distance and buildability constraints, this value is updated during the optimization process to avoid underestimation from the p-norm approximation and to capture the true required minimal angle. Denoting the prescribed minimal allowable angle by θ^*, the parameter $\tilde{\theta}^*$ is evaluated as

$$\tilde{\theta}^* = \theta^* \frac{\theta_{\text{Actual\_Min}}}{\theta_{\min\text{-}p\text{norm}}}, \tag{31}$$

where $\theta_{\text{Actual\_Min}}$ denotes the actual minimal angle.

7.5. Overall formulation

The complete optimization problem is formed by combining the objective function and all constraints introduced above, stated as

$$
\begin{aligned}
\min_{\mathbf{X},T_b,v} \quad & \tilde{\phi} = \frac{w_1}{\phi_1^0}\underbrace{(\mathbf{l}\circ\mathbf{u}_{sp\tilde{d}})^T(\mathbf{l}\circ\mathbf{u}_{sp\tilde{d}})}_{\phi_1} + \frac{w_2}{\phi_2^0}\underbrace{\mathbf{f}_{\tilde{\tilde{d}}l}^T\mathbf{u}_{\tilde{\tilde{d}}l}}_{\phi_2} + \frac{w_3}{\phi_3^0}\underbrace{\mathbf{T}}_{\phi_3} + \frac{w_4}{\phi_4^0}\underbrace{L_T/v}_{\phi_4} \\
\text{s.t.} \quad & g_1 = V/V^* - 1 \le 0 \\
& g_2 = R^{\text{seg}}_{\text{max-}p\text{norm}}/\tilde{R}^* - 1 \le 0 \\
& g_3 = -d_{\text{min-}p\text{norm}}/\tilde{d}^* + 1 \le 0 \\
& g_4 = -\theta_{\text{min-}p\text{norm}}/\tilde{\theta}^* + 1 \le 0 \\
& \underline{\mathbf{X}} \le \mathbf{X} \le \overline{\mathbf{X}} \\
& \underline{\mathbf{T}} \le \mathbf{T} \le \overline{\mathbf{T}} \\
& \underline{v} \le v \le \overline{v} \\
\text{with:} \quad & \mathbf{K}\,\mathbf{u}_{sp\tilde{d}} = \mathbf{f}_{sp\tilde{d}}, \\
& \mathbf{K}\,\mathbf{u}_{\tilde{\tilde{d}}l} = \mathbf{f}_{\tilde{\tilde{d}}l}.
\end{aligned}
\tag{32}
$$

where $\underline{\mathbf{X}}$ and $\overline{\mathbf{X}}$ denote the lower and upper admissible bounds on the control-point coordinates, $\underline{\mathbf{T}}$ and $\overline{\mathbf{T}}$ define the lower and upper bounds on the total prestressing force, and $\underline{v}$ and $\overline{v}$ specify the admissible range of the printing speed. In this work, we choose to fix the volume and minimize displacement—rather than fixing displacement and minimizing volume—because the former provides a more stable optimization procedure, allowing us to introduce the new methodology without unnecessary difficulties. A reorganization of the formulation, including displacement-limited and volume-minimizing variants, is in principle possible but is left for future exploration.

8. Sensitivity analysis

The proposed optimization framework is gradient-based, requiring rigorous sensitivity analysis of the objective function and constraints in (32) with respect to the design variables. The first two components of the objective function, ϕ_1 and ϕ_2, depend on the design variables implicitly through the physical responses $\mathbf{u}_{(\cdot)}$, referred to as the state variables, which makes direct differentiation expensive. For this reason, we employ the adjoint method to differentiate these terms, removing the implicit dependence and enabling efficient sensitivity evaluation. The remaining component of the objective function and all constraints can be differentiated explicitly using the chain rule.

We start by deriving the sensitivity of the objective function. Following the adjoint approach, we formulate the augmented objective, which incorporates the linear systems required to solve

the underlying physical problems,

$$\hat{\phi} = \frac{w_1}{\phi_1^0} \underbrace{(\mathbf{l} \circ \mathbf{u}_{spd\tilde{}})^T (\mathbf{l} \circ \mathbf{u}_{spd\tilde{}})}_{\phi_1} + \frac{w_2}{\phi_2^0} \underbrace{\mathbf{f}_{\tilde{\tilde{d}}l}^T \mathbf{u}_{\tilde{\tilde{d}}l}}_{\phi_2} + \frac{w_3}{\phi_3^0} \underbrace{\mathbf{T}}_{\phi_3} + \frac{w_4}{\phi_4^0} \underbrace{L_T/v}_{\phi_4} + \boldsymbol{\lambda}_1^T(\mathbf{K}\,\mathbf{u}_{spd\tilde{}} - \mathbf{f}_{spd\tilde{}}) + \boldsymbol{\lambda}_2^T(\mathbf{K}\,\mathbf{u}_{\tilde{\tilde{d}}l} - \mathbf{f}_{\tilde{\tilde{d}}l}), \tag{33}$$

where $\boldsymbol{\lambda}_1$ and $\boldsymbol{\lambda}_2$ are the adjoint vectors. Differentiating Eq. (33) with respect to the design variables $\tilde{\mathbf{X}} = [\,\mathbf{X},\,\mathbf{T},\,v\,]$ yields

$$\begin{aligned}
\frac{d\hat{\phi}}{d\tilde{\mathbf{X}}} &= 2\,\frac{w_1}{\phi_1^0}\,\big(\mathbf{l} \circ \mathbf{u}_{spd\tilde{}}\big)^T \mathbf{l} \circ \left(\frac{\partial \mathbf{u}_{spd\tilde{}}}{\partial \tilde{\mathbf{X}}}\right) + \frac{w_2}{\phi_2^0}\,\mathbf{f}_{\tilde{\tilde{d}}l}^T\,\frac{\partial \mathbf{u}_{\tilde{\tilde{d}}l}}{\partial \tilde{\mathbf{X}}} \\
&\quad + \frac{w_3}{\phi_3^0}\,\frac{\partial \mathbf{T}}{\partial \tilde{\mathbf{X}}} + \frac{w_4}{\phi_4^0}\left[\frac{1}{v}\,\frac{\partial L_T}{\partial \tilde{\mathbf{X}}} - \frac{L_T}{v^2}\,\frac{\partial v}{\partial \tilde{\mathbf{X}}}\right]. \\
&\quad + \boldsymbol{\lambda}_1^T\Big(\frac{\partial \mathbf{K}}{\partial \tilde{\mathbf{X}}}\,\mathbf{u}_{spd\tilde{}} + \mathbf{K}\,\frac{\partial \mathbf{u}_{spd\tilde{}}}{\partial \tilde{\mathbf{X}}} - \frac{\partial \mathbf{f}_{spd\tilde{}}}{\partial \tilde{\mathbf{X}}}\Big) \\
&\quad + \boldsymbol{\lambda}_2^T\Big(\frac{\partial \mathbf{K}}{\partial \tilde{\mathbf{X}}}\,\mathbf{u}_{\tilde{\tilde{d}}l} + \mathbf{K}\,\frac{\partial \mathbf{u}_{\tilde{\tilde{d}}l}}{\partial \tilde{\mathbf{X}}}\Big)
\end{aligned} \tag{34}$$

where we assume that the dead and live loads in the term $\mathbf{f}_{\tilde{\tilde{d}}l}$ are independent of the design variables $\tilde{\mathbf{X}}$.

The implicit derivatives of the state variables with respect to $\mathbf{X}$ are eliminated by introducing the adjoint vectors $\boldsymbol{\lambda}_1$ and $\boldsymbol{\lambda}_2$, chosen such that all implicit terms cancel, leaving only explicit derivatives in the final sensitivity expression. By collecting the terms multiplying $\partial \mathbf{u}_{spd\tilde{}}/\partial \mathbf{X}$ and $\partial \mathbf{u}_{\tilde{\tilde{d}}l}/\partial \mathbf{X}$ and setting them to zero, we obtain the following adjoint equations:

$$\mathbf{K}^T \boldsymbol{\lambda}_1 = -2\,\frac{w_1}{\phi_1^0}\,\big(\mathbf{l} \circ \mathbf{u}_{spd\tilde{}} \circ \mathbf{l}\big), \tag{35}$$

$$\mathbf{K}^T \boldsymbol{\lambda}_2 = -\frac{w_2}{\phi_2^0}\,\mathbf{f}_{\tilde{\tilde{d}}l}. \tag{36}$$

The second adjoint equation arises from a self-adjoint term, meaning that we can directly set

$$\boldsymbol{\lambda}_2 = -\frac{w_2}{\phi_2^0}\,\mathbf{u}_{\tilde{\tilde{d}}l}, \tag{37}$$

without the need to solve it explicitly. Thus, only the first adjoint equation (35) remains to be solved to obtain $\boldsymbol{\lambda}_1$.

Having $\boldsymbol{\lambda}_1$ and $\boldsymbol{\lambda}_2$, substitution back into Eq. (34) yields the final expression for the design

sensitivities containing only explicit derivatives,

$$\begin{aligned}\frac{d\hat{\phi}}{d\tilde{\mathbf{X}}} = \frac{w_3}{\phi_3^0}\frac{\partial \mathbf{T}}{\partial \tilde{\mathbf{X}}} + \frac{w_4}{\phi_4^0}\left[\frac{1}{v}\frac{\partial L_T}{\partial \tilde{\mathbf{X}}} - \frac{L_T}{v^2}\frac{\partial v}{\partial \tilde{\mathbf{X}}}\right] \\ + \boldsymbol{\lambda}_1^T\Big(\frac{\partial \mathbf{K}}{\partial \tilde{\mathbf{X}}}\mathbf{u}_{sp\tilde{d}} - \frac{\partial \mathbf{f}_{sp\tilde{d}}}{\partial \tilde{\mathbf{X}}}\Big) \\ + \boldsymbol{\lambda}_2^T\Big(\frac{\partial \mathbf{K}}{\partial \tilde{\mathbf{X}}}\mathbf{u}_{\tilde{d}l}\Big).\end{aligned} \tag{38}$$

The components appearing in the above equations can be evaluated explicitly through the following relations:

- $\frac{\partial \mathbf{T}}{\partial \tilde{\mathbf{X}}}$ and $\frac{\partial v}{\partial \tilde{\mathbf{X}}}$: Since $\mathbf{T}$ and v are independent design variables, their sensitivities reduce to $\frac{\partial \mathbf{T}}{\partial \mathbf{T}} = \mathbf{1}$ and $\frac{\partial v}{\partial v} = 1$, respectively.
- $\frac{\partial L_T}{\partial \tilde{\mathbf{X}}}$: Because the total toolpath length L_T depends only on the geometry, we have $\frac{\partial L_T}{\partial \tilde{\mathbf{X}}} = \frac{\partial L_T}{\partial \mathbf{X}}$, computed by differentiating Eq. (4) together with the curve extraction procedure in Section 3.3.
- $\frac{\partial \mathbf{K}}{\partial \tilde{\mathbf{X}}}$: This is the derivative of the stiffness matrix $\mathbf{K}$ with respect to the shape design variables. As noted in Section 6, the stiffness matrix is related to the shape design variables through the density field $\boldsymbol{\rho}$, which depends only on the shape design variables $\mathbf{X}$. Accordingly, the derivative can be expressed as
$$\frac{\partial \mathbf{K}}{\partial \tilde{\mathbf{X}}} = \frac{\partial \mathbf{K}}{\partial \boldsymbol{\rho}}\frac{\partial \boldsymbol{\rho}}{\partial \mathbf{X}}.$$
- $\frac{\partial \mathbf{f}_{sp\tilde{d}}}{\partial \tilde{\mathbf{X}}}$: This term represents the derivative of the combined self-weight, prestressing, and dead-load force vector $\mathbf{f}_{sp\tilde{d}}$ with respect to the design variables $\tilde{\mathbf{X}}$. The dead-load component $\mathbf{f}_{\tilde{d}}$ does not depend on the design variables, and therefore its derivative vanishes. The derivative with respect to the shape design variables arises from both the self-weight and the prestressing forces,
$$\frac{\partial \mathbf{f}_{sp\tilde{d}}}{\partial \mathbf{X}} = \frac{\partial \mathbf{f}_s}{\partial \boldsymbol{\rho}}\frac{\partial \boldsymbol{\rho}}{\partial \mathbf{X}} + \frac{\partial \mathbf{f}_p}{\partial \mathbf{X}}.$$
The derivative with respect to the prestressing forces arises only from $\mathbf{f}_p$,
$$\frac{\partial \mathbf{f}_{sp\tilde{d}}}{\partial \mathbf{T}} = \frac{\partial \mathbf{f}_p}{\partial \mathbf{T}}.$$
Neither of the forces depends on the printing speed, and therefore
$$\frac{\partial \mathbf{f}_{sp\tilde{d}}}{\partial v} = 0.$$

Regarding the constraints, they all depend explicitly on the design variables through the sequence of explicit relations presented in the previous sections, where their derivatives are consistently developed following the chain rule.

9. Examples

In this section, we present applications of the proposed methodology to prestressed beam and slab examples and examine the influence of various design aspects, including buildability constraints. The physical dimensions, material properties, and loads are chosen to reflect realistic design conditions.

The material parameters are set to $E = 3 \cdot 10^7\,\mathrm{kN/m^2}$ and $\nu = 0.2$. The weight of concrete is assumed as $25\,\mathrm{kN/m^3}$ for computing the self-weight. The correction factor f_{AR} in Eq. (19) is taken as 1.3, and the dead-load factor w_d in Eq. (11) is set to 0.5. The linear system of equations arising in the analysis is solved using a three-level multigrid scheme, following the implementation of Shakur et al. (2024). Throughout the examples, l_x, l_y, and l_z denote the length, width, and height of the design domain, respectively, corresponding to the span, width, and thickness of the structural component.

The optimization is performed using the Method of Moving Asymptotes (MMA) by Svanberg (1987). The process is terminated when the absolute change in both the objective function and the constraints between consecutive iterations falls below 0.002 for four successive iterations. Numerical experiments revealed a slightly volatile behavior in the distance constraint (as demonstrated later for the beam example); therefore, the stopping criterion for this specific constraint is relaxed to 0.02. The maximum number of iterations is limited to 100. Design updates within each iteration are restricted by move limits as follows: 1 cm for the shape variables, 1 cm/s for the printing velocity, and 10 kN for the prestressing force. The vector $\mathbf{l}$ in Eq. (12) is constructed to activate all vertical displacements at the top surface. The exponents of the p-norm used for the buildability distance and angle constraints, p_b, p_d, and p_θ (associated with g_2, g_3, and g_4), are all set to 12. The volume fraction V_{frac} that is the ratio between the allowable volume V^* and the volume of the design domain, is limited to 50%.

The initial printing speed used for formulating the buildability constraint is 11 cm/s. The minimum and maximum allowable printing speeds are 0.08 m/s and 0.15 m/s, respectively. For considering buildability, the structures are divided into segments that are 2 m long. Four concrete mixtures with fiber contents of 0%, 0.3%, 0.375%, and 0.45% are used in the numerical examples. The corresponding material parameters are listed in the Appendix. The toolpath is generated assuming cross-sectional sizes of 0.01×0.02 m with a 10% overlap between successive layers. While these parameters reflect the technological conditions of the specific facility that is expected to perform printing experiments, the methodology is general and can be applied to a wide range of printing parameters. The printing direction of each segment is assumed to

proceed from the mid-length of the design outward, since the cross-section is expected to be largest near the mid-length and to become smaller toward the design ends.

Following the parameterization of Section 4, the cable groups are positioned at a fixed offset of $d_{\text{cable}} = 0.05$ m from the outer surface. To estimate the required number of prestressing cables in each group, we assume the use of cables with a diameter of $\frac{1}{2}$ inch ≈ 1.27 cm, each providing a maximum prestressing capacity of approximately 180 kN.

9.1. Simply-supported beam

In this example, we demonstrate the applicability of the proposed approach on a simply-supported beam. The beam domain has a length-to-height ratio of 13.333:1, with a span of 8 m and a cross-section of $0.6 \times 0.6\,\text{m}^2$. The dead and live loads are both set to $30\,\text{kN/m}$ and are uniformly distributed along the upper chord of the beam. Exploiting the double symmetry of the problem, only a quarter of the domain is modeled and optimized. The model is discretized using cube-shaped finite elements of size 0.025 m, resulting in a mesh of $160 \times 12 \times 24$ elements. The setup of the numerical model is shown in Figure 9. In this example, the minimum distance and angle between the cross-sectional control points of the outer surface are set to 0.07 m and 70°, corresponding to the constraints g_3 and g_4 in the optimization, respectively. The objective weights are chosen as $w_1 = w_2 = w_3 = w_4 = 0.25$.

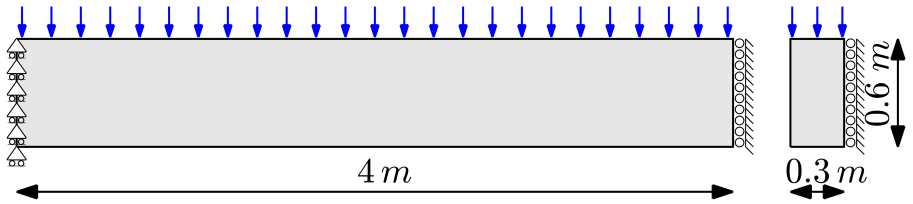

Figure 9: Problem setup for a quarter-symmetric portion of the simply supported beam.

Prestressing force

The beam contains one group of prestressing cables stretched along the bottom chord in the mid-width region, and two prestressing cables placed in the upper chords, as described in Section 4. The prestressing force in each cable located in the upper chord is fixed and set to 50 kN. To estimate the total prestressing force required in the bottom chord, we compute the force necessary to balance the bending moment at the mid-span cross-section, assuming that the entire beam height is effective at this location. This equilibrium condition is evaluated with respect to the first part of the objective function, which accounts for the self-weight (with $V_{\text{frac}} = 0.5$) and a portion of the dead load ($\mathbf{f}_{\tilde{d}} = w_d \cdot f_d$). Assuming a uniform distribution of these loads, the equivalent load can be computed as

$$q_{\text{equ}} = \left(V_{\text{frac}}\,\gamma_c\,l_z\,l_y + w_d\,q_d\right) = (0.5 \times 25 \times 0.6 \times 0.6 + 0.5 \times 30) = 19.5\ \text{kN/m}.$$

Assuming the full height of the beam and an eccentricity of $e_{\max} = 0.25$m for the upper and bottom cables, the balancing force is computed as

$$T_p = \frac{q_{\text{equ}}\, l_x^2}{8\, e_{\max}} + 2\, T_{\text{upper Cables}} = \frac{19.5 \cdot 8^2}{8 \cdot 0.25} + 2 \cdot 50 = 724 \text{ kN}. \tag{39}$$

This value is used to determine the initial prestressing force for the optimization. Since only the quarter-symmetric part of the beam is modeled, and the cables lie within the mid-width symmetry plane, the corresponding force applied in the numerical model is half of the full prestressing force, i.e., $T_{p,\text{initial}} = 362\,\text{kN}$. The box constraints are defined as $\overline{T_b} = T_{p,\text{initial}}$ and $\underline{T_b} = 50\,\text{kN}$. We note that this maximum value is very close to the capacity of two prestressing cables with 180 kN each, which would correspond to four to five prestressing cables in the full design if this limit were to be reached.

Outer surface

The outer surface of the beam is constructed using a control polygon consisting of 8×9 control points, with eight points in the longitudinal direction and nine points in the cross-sectional direction. All layers of control points share the same initial configuration in the yz-plane, given in Table 2. The corresponding x-coordinates of the longitudinal layers are [0.000, 0.333, 1.000, 1.667, 2.333, 3.000, 3.667, 4.000] m.

y [m]	z [m]
0.000	0.000
0.100	0.000
0.112	0.125
0.125	0.249
0.137	0.374
0.150	0.498
0.300	0.498
0.300	0.523
0.300	0.600

Table 2: Initial yz-plane configuration of the control points for one cross-sectional layer of the outer surface representing the beam example.

The initial control polygon is illustrated in Figure 10a. The resulting geometry of the outer surface, together with its symmetric counterpart in the width direction, is presented in Figure 10b, where the prestressing cables are indicated by the green cylindrical curves.

Optimization

To examine the effect of the buildability constraint, the optimization was performed twice: first without the constraint, and then with the constraint activated. For the case including

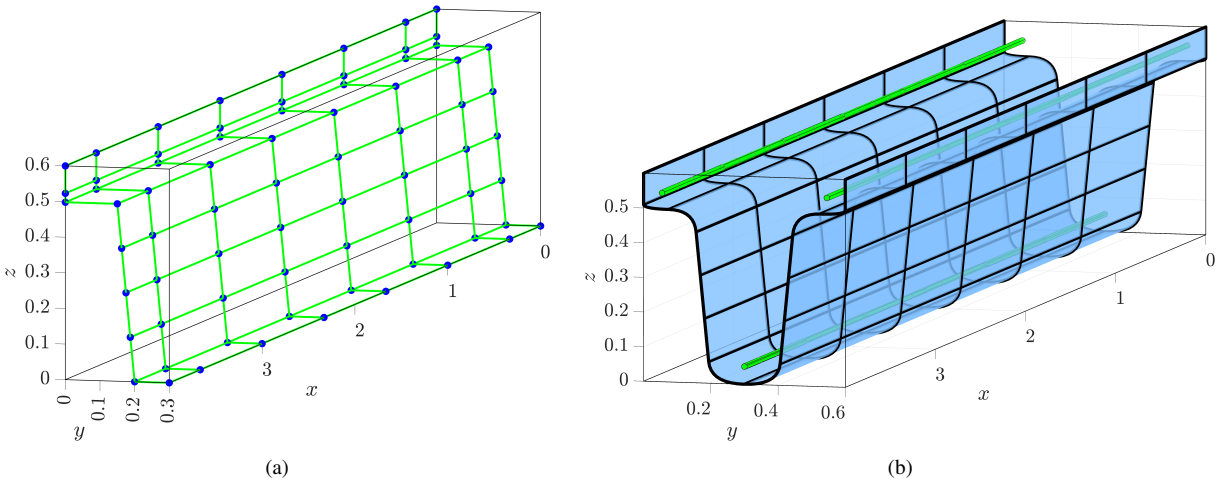

(a) (b)

Figure 10: Initial configuration of the beam: (a) control polygon, (b) outer surface of the beam (half span). The prestressing cables are shown in green.

the buildability constraint, the beam length was divided into segments of 2 m and a fiber-free mixture (0%) was selected to challenge the optimization as much as possible. In both optimization runs, the algorithm terminated after 39 and 59 iterations, respectively. The objective function decreased smoothly in both cases, and all constraints were satisfied. The corresponding convergence graphs are shown in Figure 11. An oscillatory behavior is observed in the distance constraint, caused by the optimizer attempting to collapse control points onto one another. For this reason, the termination criterion associated with this constraint was slightly relaxed, as mentioned above.

The optimized control polygons are shown in Figure 12, while the corresponding outer surfaces of the half-symmetric part in both cases are presented in Figure 13. Additionally, Figure 14 illustrates the control polygon and the corresponding B-spline boundary curve in the cross-sectional direction for the initial configuration (light colors), the optimized case without the constraint (dashed lines), and the optimized case with the constraint (solid lines).

It can be observed that, in both cases, the beam increases its height in the mid-span region, thereby increasing the cable eccentricity, while a reduced height is obtained toward the beam ends. The geometric differences between the two cases can be seen in Figure 14, with relatively pronounced variations toward the beam ends, indicating that the optimization tends to shorten the toolpath in these regions when the buildability constraint is applied. A more detailed qualitative comparison is provided later in this section.

Examination of buildability

To examine the effect of the buildability constraint, we assessed the buildability of the design obtained without the constraint, with four combinations of fiber-enhanced mixtures at a printing velocity of 15 cm/s and a beam segment length of 2 m. Each segment contains 222 3D-printed layers, which, according to Eq. (20), results in 49,506 time points at which the stress is compared

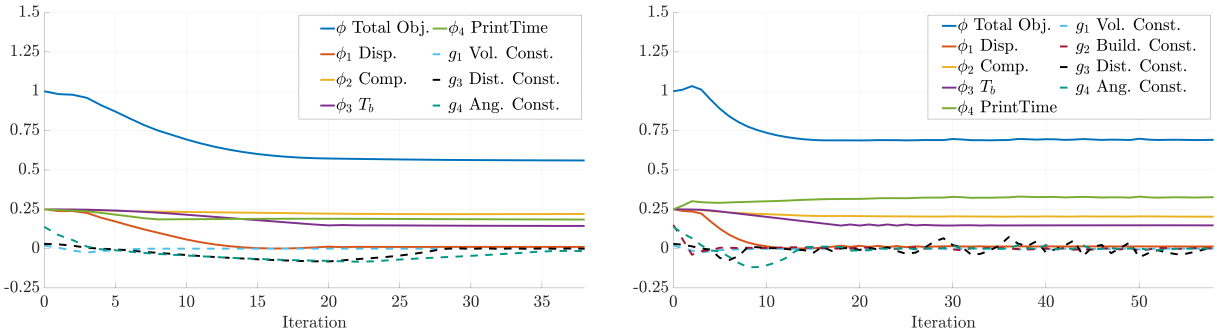

Figure 11: Convergence graphs of the optimization process for the beam example. (a) Without the buildability constraint activated, and (b) with the buildability constraint activated.

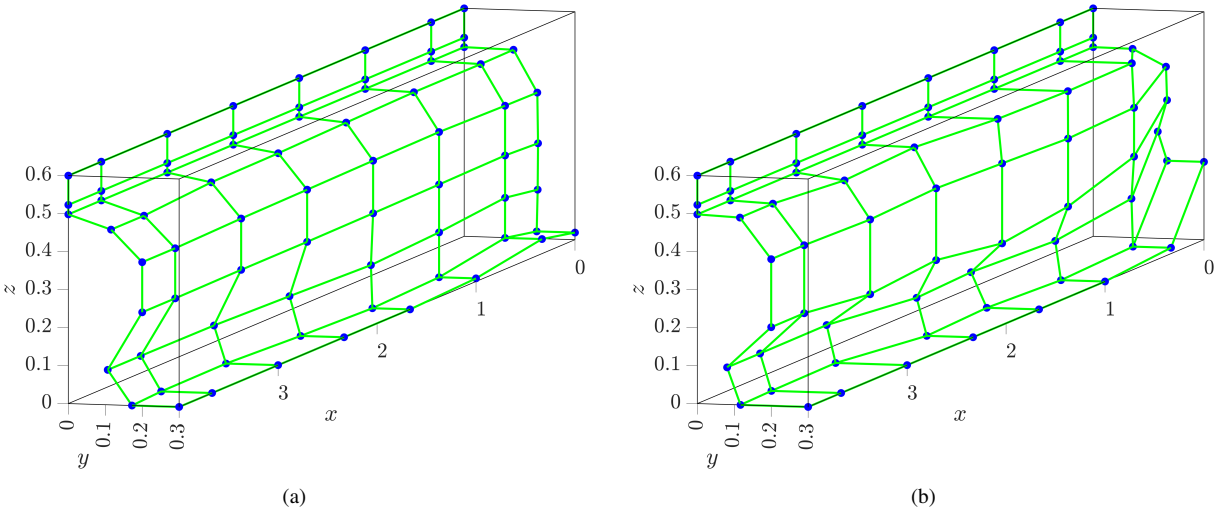

Figure 12: Optimized control polygon of the beam. (a) Without the buildability constraint activated, and (b) with the buildability constraint activated.

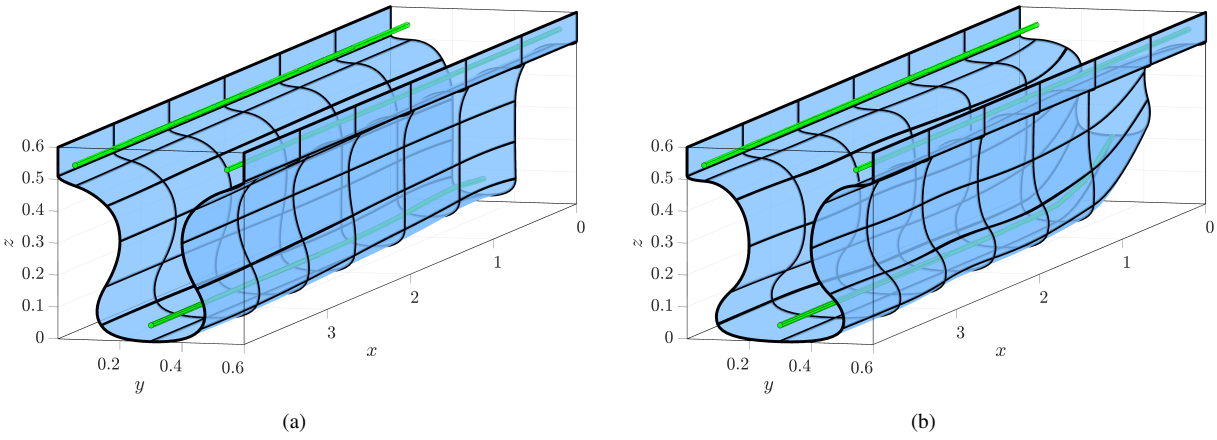

Figure 13: Optimized outer surface of the beam. (a) Without the buildability constraint activated, and (b) with the buildability constraint activated.

against the allowable stress.

Figure 15 illustrates the buildup of layer stress together with the evolution of the static yield stress over time for the examined mixtures. The blue line represents the material's static yield

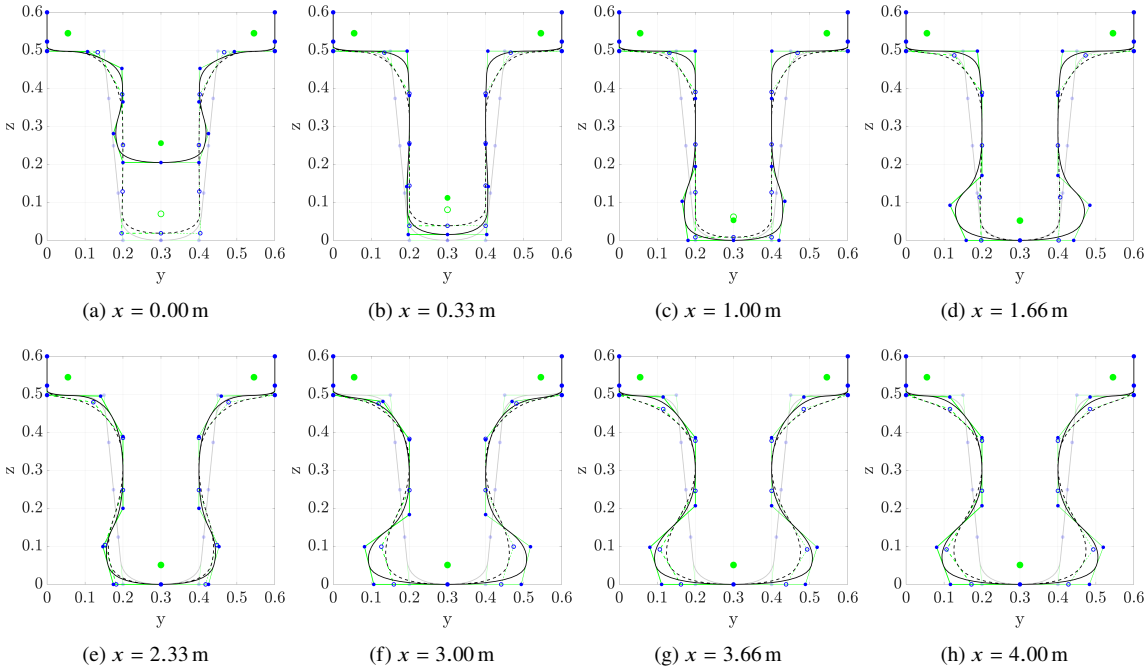

Figure 14: Control polygons and corresponding B-spline boundary curves in the cross-sectional direction for the beam example. Initial configuration (light colors); optimized case without the buildability constraint (dashed lines, control points shown as hollow blue circles and cables as hollow green circles); and optimized case with the buildability constraint (solid lines, control points shown as filled blue circles and cables as filled green circles).

stress as a function of time, while the black lines indicate the cumulative stress in each layer, with each line corresponding to one layer. The layer with the most stress checks is the first 3D-printed layer in each segment, as its stress is evaluated at the time step when each of the other layers in the segment is deposited. The lines representing the accumulated stress in the first layers of the two segments are shown in dashed red line.

The graphs in Figure 15 show that for the first three mixtures, with fiber contents of 0%, 0.3%, and 0.375%, the black lines intersect the blue line at some point, indicating potential collapse. In contrast, for the 0.45% fiber mixture, no intersection is observed, meaning that no collapse is expected. Although the beam can be 3D-printed without potential collapse when using the mixture with 0.45% fibers, our goal is for the procedure to generate designs and parameters that are also buildable with lower fiber contents, as these are more economical. Nevertheless, given the fact that mixtures with lower fiber content may require longer printing times, which could be considered less economical, we note that a certain freedom remains for the designers to choose the appropriate trade-off between material cost and printing time, depending on specific cost factors.

Focusing on the first graph corresponding to the fiber-free mixture (0%), we further examine the effects of varying the segment length and the printing speed. When analyzing the first segment in detail, the collapse occurred at the first printed layer, immediately after the 36^{th} layer was completed, with a time difference of 21.55 minutes between the printing of these two layers. This observation indicates that avoiding failure through segmentation alone is challenging, as it

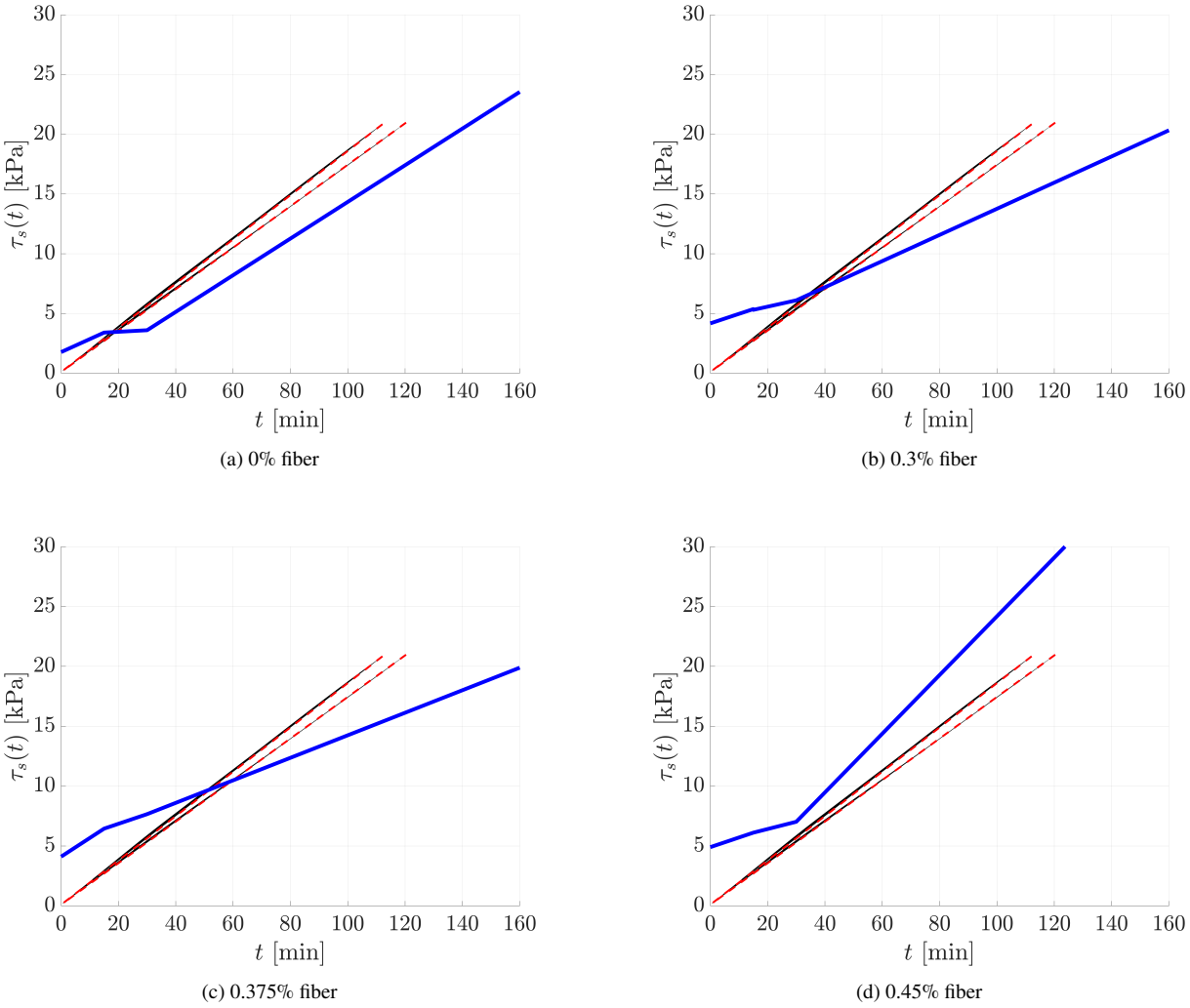

(a) 0% fiber

(b) 0.3% fiber

(c) 0.375% fiber

(d) 0.45% fiber

Figure 15: Buildup of layer stress and evolution of static yield stress over time for the examined mixtures. The blue line represents the material's static yield stress as a function of time, while the black lines indicate the cumulative stress in each layer. The dashed red lines highlight the accumulated stress in the first layers of the two segments.

would require segment lengths shorter than 36 layers, corresponding to approximately 32 cm. Such short segments would make the beam more difficult to assemble, though this has been achieved in previous realizations (Vantyghem et al., 2020).

Figure 16 presents the buildability graph for the design obtained when the buildability constraint is activated for the fiber-free mixture, demonstrating that the resulting design satisfies the buildability requirements. This is achieved by the optimization through reducing the printing velocity to 9.34 cm/s and by modifying the geometry of the outer surface, as shown in Figure 14.

To evaluate buildability during optimization, the toolpath length in each printed layer is estimated using the linear approximation defined in Eq. (4) (see Section 5.2). The corresponding parameters are set to $a = 6.95$ and $b = -1.23$ m and are identified by evaluating the toolpath length of each layer in the optimization without the buildability constraint. A comparison between the sampled toolpath lengths and their linear approximation is shown in Figure 17.

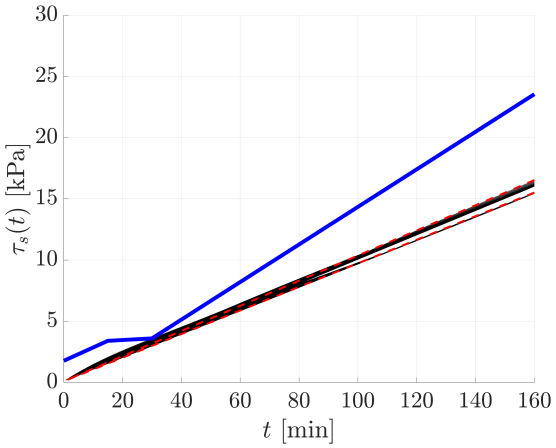

Figure 16: Buildability graph obtained by activating the buildability constraint for the zero-fiber (0%) mixture. The blue line represents the material's static yield stress as a function of time, while the black lines indicate the cumulative stress in each printed layer.

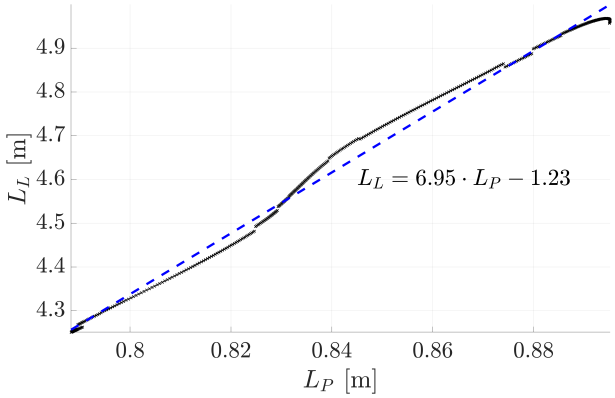

Figure 17: Linear approximation of the toolpath length per layer using parameters $a = 6.95$ and $b = -1.23$. Sampled values of the actual toolpath length are shown together with the corresponding linear fit.

Quantitative overview

For a more quantitative overview of the different cases, Table 3 summarizes the key measures for the initial and optimized designs. The table shows that the total scaled objective $\tilde{\phi}$ decreases from 1.000 to 0.560 in the case without the buildability constraint, and to 0.691 when the buildability constraint is activated. The increase in $\tilde{\phi}$ between these two optimized cases is primarily due to the longer printing time required when the buildability constraint is enforced.

The weighted component associated with ϕ_1 $\left(w_1\,\phi_1/\phi_1^0\right)$ is reduced from 0.25 to 1.11e-02 and 1.38e-02 in the two optimized cases, respectively, demonstrating that the optimization leads the design toward a more balanced configuration in terms of the absolute displacement along the upper chord of the beam. A more detailed analysis of this balancing effect is presented later in the text. The second component of the objective—the compliance ϕ_2—is also reduced, indicating an increase in the overall stiffness of the optimized structures.

The third component, associated with the prestressing force, is also decreased. This leads to a reduction in the prestressing force used in the numerical model from 362 kN in the initial configuration to 208.66 kN and 214.01 kN in the two optimized cases. This indicates that

less prestressing force is required to counteract the portion of the applied loads selected to be balanced. In the full design, these values correspond to 417.32 kN and 428.02 kN, respectively. Assuming a maximum capacity of approximately 180 kN per prestressing cable, three cables would be required to provide the necessary prestressing force in both optimized cases, with each cable carrying roughly 140–145 kN.

The fourth objective component, ϕ_4, represents the total printing time. The initial design requires approximately 5 h 16 min to print. In the case without the buildability constraint, this duration decreases to about 3 h 53 min because the printing speed—treated as a design variable—increases from 11 cm/s to the maximum allowable value of 15 cm/s, as expected. Conversely, when the buildability constraint is activated, the printing time increases to approximately 6 h 53 min, as the optimized printing speed is reduced to 9.34 cm/s. For the full design, this corresponds to a total printing time of about 13 h 46 min. The length of the toolpath in the full design obtained in the two cases is 4203.4 m and 4630.6 m, with corresponding volumes of 3D-printed material of 0.841 m^3 and 0.926 m^3, respectively. Finally, all constraints are satisfied in both optimized cases, with their evaluated values converging toward zero.

Measure	**Initial**	**Optimized (without build.)**	**Optimized (with build.)**
$\tilde{\phi}$	1.00	0.560	0.691
$w_1\,\phi_1/\phi_1^0$	0.250	1.11e-02	1.38e-02
$w_2\,\phi_2/\phi_2^0$	0.250	0.220	0.203
$w_3\,\phi_3/\phi_3^0$	0.250	0.144	0.148
$w_4\,\phi_4/\phi_4^0$	0.250	0.185	0.327
ϕ_1 [m^2]	1.62e-02	7.21e-04	8.96e-04
ϕ_2 [kN·m]	0.841	0.740	0.682
ϕ_3 [kN]	362.0	208.66	214.01
ϕ_4	5h 16min	3h 53min	6h 53min
v [cm/s]	11.0	15.0	9.34
T_b [kN]	362.0	208.66	214.01
g_1	1.95e-02	-9.80e-06	-2.39e-04
g_2	0.150	0	1.72e-03
g_3	0.0305	-7.71e-04	1.33e-02
g_4	0.1386	-1.52e-02	-4.94e-04
N iteration	–	39	59

Table 3: Key measures for the initial and optimized beam designs.

Load-balancing effect

To further investigate the balancing effect of the prestressing forces, the displacement profiles along the mid-width upper chord of the beam, corresponding to the different combinations of

applied forces, are shown in Figure 18. The maximum deformation associated with each load combination is reported in parentheses. The results shown correspond to the case in which the buildability constraint is activated.

It can be observed that the maximum deformation due to the self-weight and the portion of the dead load to be balanced, $\mathbf{u}_{s\tilde{d}} = -0.005\,\text{m}$, is counteracted by the prestressing-induced deformation of $\mathbf{u}_p = +0.004\,\text{m}$. This results in a combined displacement of $\mathbf{u}_{s\tilde{d}p} = -0.001\,\text{m}$ in the downward direction, indicating a nearly balanced design configuration. The maximum displacement caused by the live load and the unbalanced portion of the dead load—which are not required to be balanced in the optimization but are indirectly reduced through compliance minimization—is $\mathbf{u}_{\tilde{\tilde{dl}}} = -0.012\,\text{m}$. Consequently, the total maximum displacement, when all force contributions are combined, is $\mathbf{u}_{spdl} = -0.013\,\text{m}$.

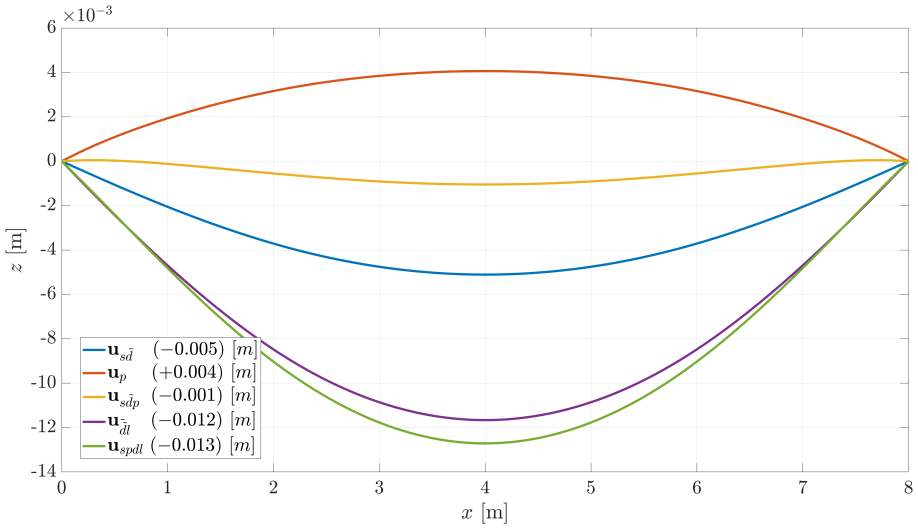

Figure 18: Deflections in the z-direction along the upper chord of the beam at mid-width, for the different loading combinations.

Toolpath illustration

Finally, we illustrate the 3D-printed geometry of the formwork for the optimized beam obtained with the buildability constraint. Figure 19 shows the 3D-printed layer profiles in the cross-sectional direction at several x-coordinates corresponding to the control points of the outer surface. Figure 20 presents a perspective view of the two printed segments that together form half of the beam span. Figure 21 illustrates side and bottom views of the two segments, laid out in the printing direction from bottom to top.

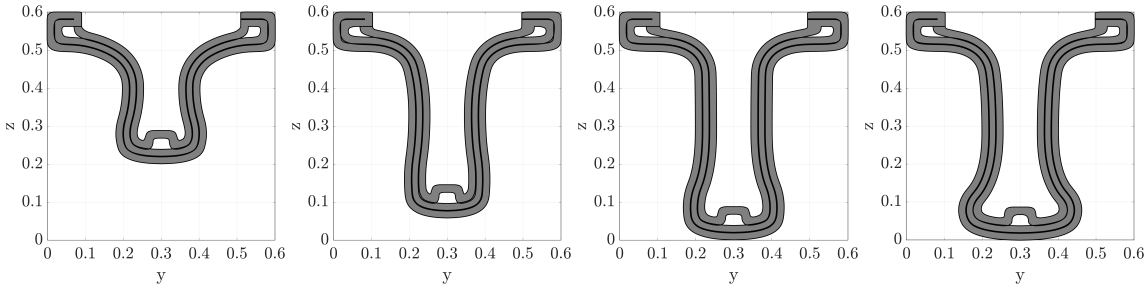

(a) $x = 0.00\,\mathrm{m}$ (b) $x = 0.33\,\mathrm{m}$ (c) $x = 1.00\,\mathrm{m}$ (d) $x = 1.66\,\mathrm{m}$

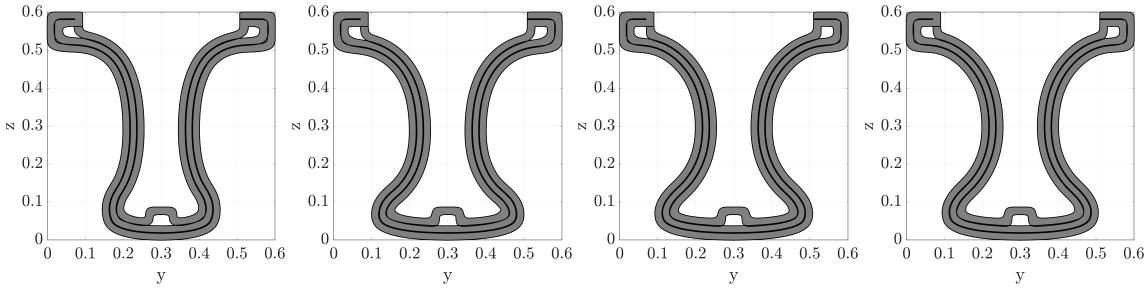

(e) $x = 2.33\,\mathrm{m}$ (f) $x = 3.00\,\mathrm{m}$ (g) $x = 3.66\,\mathrm{m}$ (h) $x = 4.00\,\mathrm{m}$

Figure 19: 3D-printed layers in the cross-sectional direction for the beam example, corresponding to the x-coordinates of the control points of the outer surface.

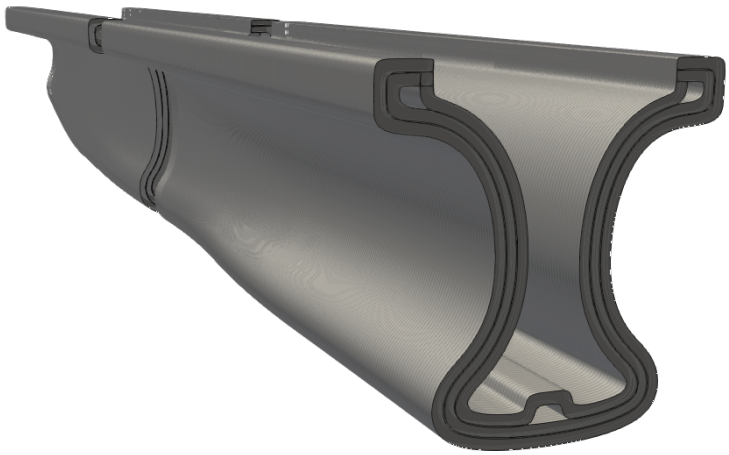

Figure 20: Perspective view of the three 3D-printed segments of the beam.

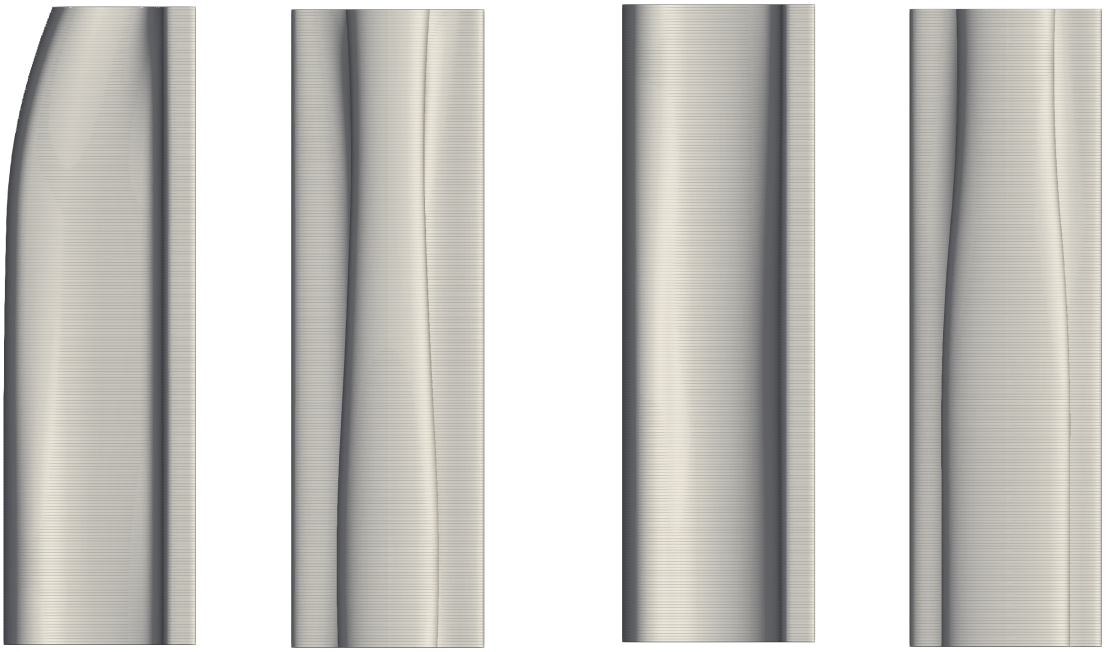

(a) Segment #1

(b) Segment #2

Figure 21: The two beam segments shown with side and bottom views. The segments are laid out in the printing direction, from bottom to top.

9.2. Simply-supported slab

In this example, we apply the proposed approach to a unidirectional simply-supported slab. The slab has overall dimensions of 12 m × 1.2 m with a maximum height of 0.36 m. Exploiting the problem's symmetry, only one quarter of the slab is modeled, corresponding to a region of 6 m × 0.6 m × 0.36 m. This region is discretized using solid cube-shaped elements with a side length of 0.03 m, resulting in a finite element mesh of 200 × 20 × 12 elements in the longitudinal, width, and height directions, respectively. The slab is subjected to uniformly distributed dead and live loads of 4 kN/m^2 and 2 kN/m^2, respectively, applied over its upper surface. The full slab contains four groups of bottom prestressing cables extending along its length, resulting in two cables within the quarter-symmetric model. The cables in the initial design are positioned at parametric values corresponding to $y = 15$ cm and $y = 45$ cm from the slab's side. The setup of the numerical model is shown in Figure 22. In this case study, the shape design variables include only the z-direction of the control points of the outer surface, as explained in Section 4. Therefore, no sharp angles or small distances are expected to be obtained. The optimization is thus carried out without the distance and angle constraints g_3 and g_4.

Numerical tests show that using uniform objective weights in this example causes the optimizer to favor reducing the prestressing force, minimized by the third objective component, at the expense of balancing the displacement governed by the first component. To avoid this imbalance, the weight of the third component is reduced to 0.1 of the others. Accordingly, we use $w_1 = w_2 = w_4 = 0.3226$ and $w_3 = 0.0323$.

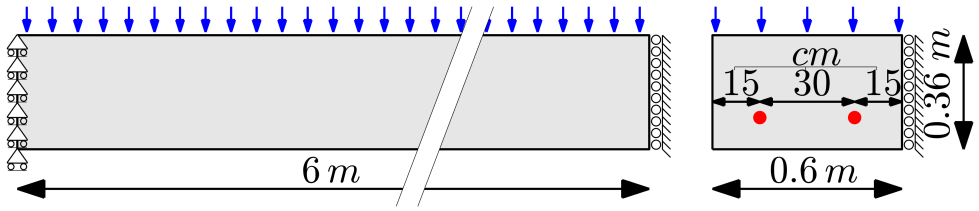

Figure 22: Problem setup for a quarter-symmetric part of the simply supported slab.

Prestressing force

Similar to the previous case, the total prestressing load in the lower part of the slab is determined by balancing the bending moments at mid-span, assuming that the full slab height is effective. This equilibrium corresponds to the first term of the objective function, which accounts for the self-weight (with $V_{\text{frac}} = 0.5$) and a portion of the dead load ($\mathbf{f}_{\tilde{d}} = w_d \cdot f_d$). Assuming a uniform distribution of the dead load $\mathbf{f}_{\tilde{d}}$ and half of the self-weight f_s, the equivalent load is given by

$$q_{\text{equ}} = \left(V_{\text{frac}}\, \gamma_c\, l_z\, l_y + w_d\, q_d\, l_y\right) = (0.5 \times 25 \times 0.36 \times 1.2 + 0.5 \times 4 \times 1.2) = 7.8 \text{ kN/m}.$$

Considering the full slab height and the prestressing cables located 0.05 m from the bottom, the maximum eccentricity at mid-span is given by $e_{\max} = \frac{0.36}{2} - 0.05 = 0.13\,\text{m}$. The corresponding balancing force in all bottom cables is then calculated as

$$T_p^{total} = \frac{q_{\text{equ}}\, l_x^2}{8\, e_{\max}} = \frac{7.8 \times 12^2}{8 \times 0.13} = 1080\ \text{kN}. \tag{40}$$

Dividing the total prestressing force among the four groups of cables located at the bottom of the slab, each group carries $1080/4 = 270\,\text{kN}$. This value is used as the initial prestressing force in both cable groups in the quarter-symmetric model. The incremental change in prestressing force is set to 10 kN. The maximum force in each group is defined as $\overline{T_b} = 360\,\text{kN}$, corresponding to the maximum capacity of two prestressing cables, and $\underline{T_b} = 50\,\text{kN}$.

The covering surface

The covering surface of the slab is constructed using a control polygon consisting of 8×10 control points, with 8 points in the longitudinal direction and 10 points in the cross-sectional direction. All layers of control points share the same initial configuration in the yz-plane, which is provided in Table 4. The corresponding x-coordinates of the longitudinal layers are $\mathbf{x} = [\,0.0,\ 0.5,\ 1.5,\ 2.5,\ 3.5,\ 4.5,\ 5.5,\ 6.0\,]$ m.

y [m]	z [m]
0.000	0.360
0.000	0.300
0.000	0.240
0.088	0.217
0.175	0.193
0.263	0.170
0.350	0.147
0.438	0.123
0.525	0.100
0.600	0.100

Table 4: Initial yz-plane configuration of the control points for one cross-sectional layer of the outer surface representing the slab example.

The initial control polygon is illustrated in Figure 23a. The resulting geometry of the outer surface, together with its symmetric counterpart in the width direction, is presented in Figure 23b, where the prestressing cables are indicated by the green cylindrical curves.

Optimization

Similar to the previous case, the optimization was executed twice—once without the buildability constraint and once with the constraint activated—to examine its effect on the resulting design. For the case including the buildability constraint, a fiber-free mixture was selected,

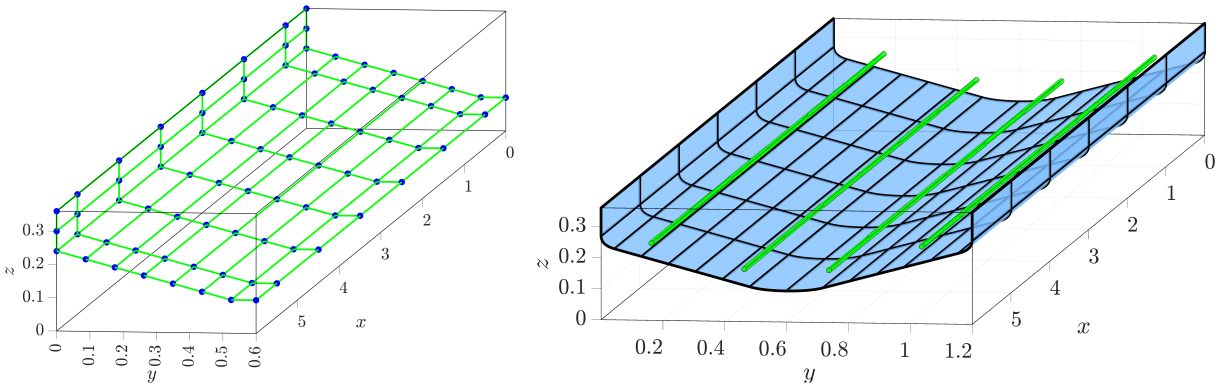

Figure 23: Initial configuration of the slab. (a) Control polygon, (b) outer surface of the beam (half span). The prestressing cables are shown in green.

and the slab length was divided into segments of 2 m. In both optimization runs, the algorithm terminated after 42 and 40 iterations, respectively. The objective function decreased smoothly in both cases, and all constraints were satisfied. The corresponding convergence graphs are shown in Figure 24.

The optimized control polygons are shown in Figure 25, while the corresponding outer surfaces of the half-symmetric part in both cases are presented in Figure 26. Additionally, Figure 27 illustrates the control polygon and the corresponding B-spline boundary curve in the cross-sectional direction for the initial configuration (light colors), the optimized case without the constraint (dashed lines), and the optimized case with the constraint (solid lines).

It can be observed that in both cases, the slab increases its height in the mid-span region, thereby increasing the stiffness and the cable eccentricity, while a reduced height is obtained toward the slab ends. The geometric differences between the two cases, shown in Figure 27, are relatively subtle. In both designs, the degrees of freedom located near the mid-width of the slab move toward positions that produce the maximum height, whereas the control points near the slab edges shift towards positions that yield the minimum height. Overall, this behavior drives the design toward a shape that resembles a T-section.

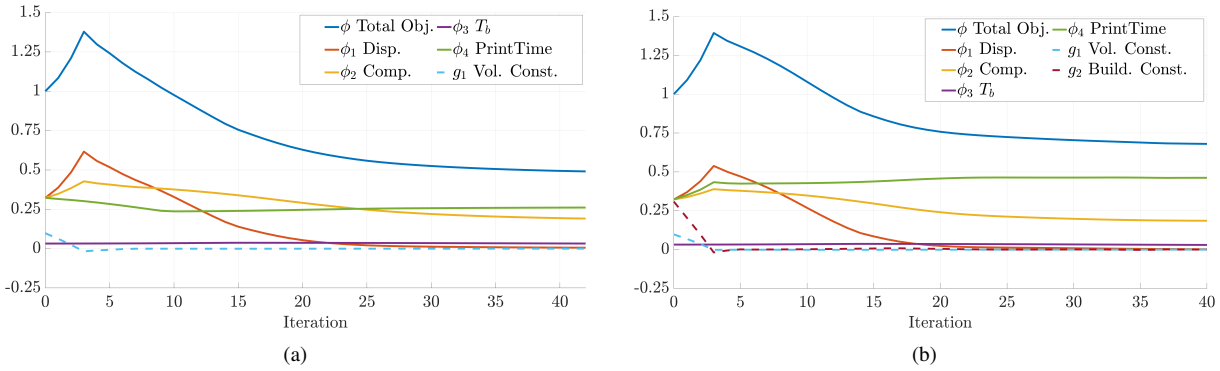

Figure 24: Convergence graphs of the optimization process for the slab example. (a) Without the buildability constraint activated, and (b) with the buildability constraint activated.

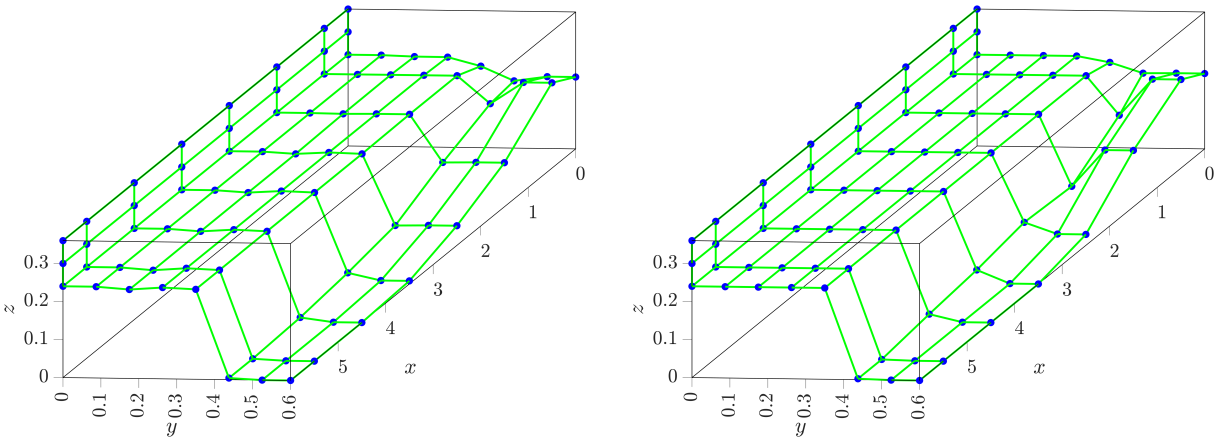

(a) (b)

Figure 25: Optimized control polygon of the slab. (a) Without the buildability constraint activated, and (b) with the buildability constraint activated.

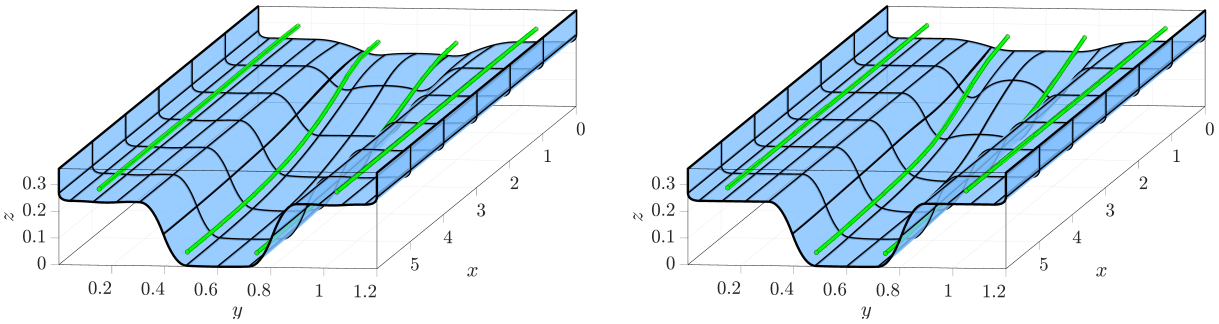

(a) (b)

Figure 26: Optimized outer surface of the slab. (a) Without the buildability constraint activated, and (b) with the buildability constraint activated.

Buildability examination

As in the previous case, we first assessed the buildability of the design obtained without activating the constraint, considering four fiber-enhanced mixtures at a printing velocity of 15 cm/s and a segment length of 2 m. Each segment contains 222 printed layers, which, according to Eq. (20), results in 74,259 time points at which the stress is checked against the allowable limit. Figure 28 illustrates the buildup of layer stress together with the evolution of the static yield stress over time for the examined mixtures. The graphs in Figure 28 show that for the first three mixtures, with fiber contents of 0%, 0.3%, and 0.375%, the black lines intersect the blue line at some point, indicating potential collapse. In contrast, for the 0.45% fiber mixture, no intersection is observed, meaning that no collapse is expected.

Figure 29 presents the buildability graph for the design obtained with the buildability constraint activated for the fiber-free mixture, demonstrating that the resulting geometry satisfies the buildability requirements. This is achieved primarily through a reduction of the printing velocity to 8.63 cm/s, accompanied by subtle adjustments to the geometry of outer surface, as shown in Figure 27. The reason for the small geometric changes lies in the imposed geometric

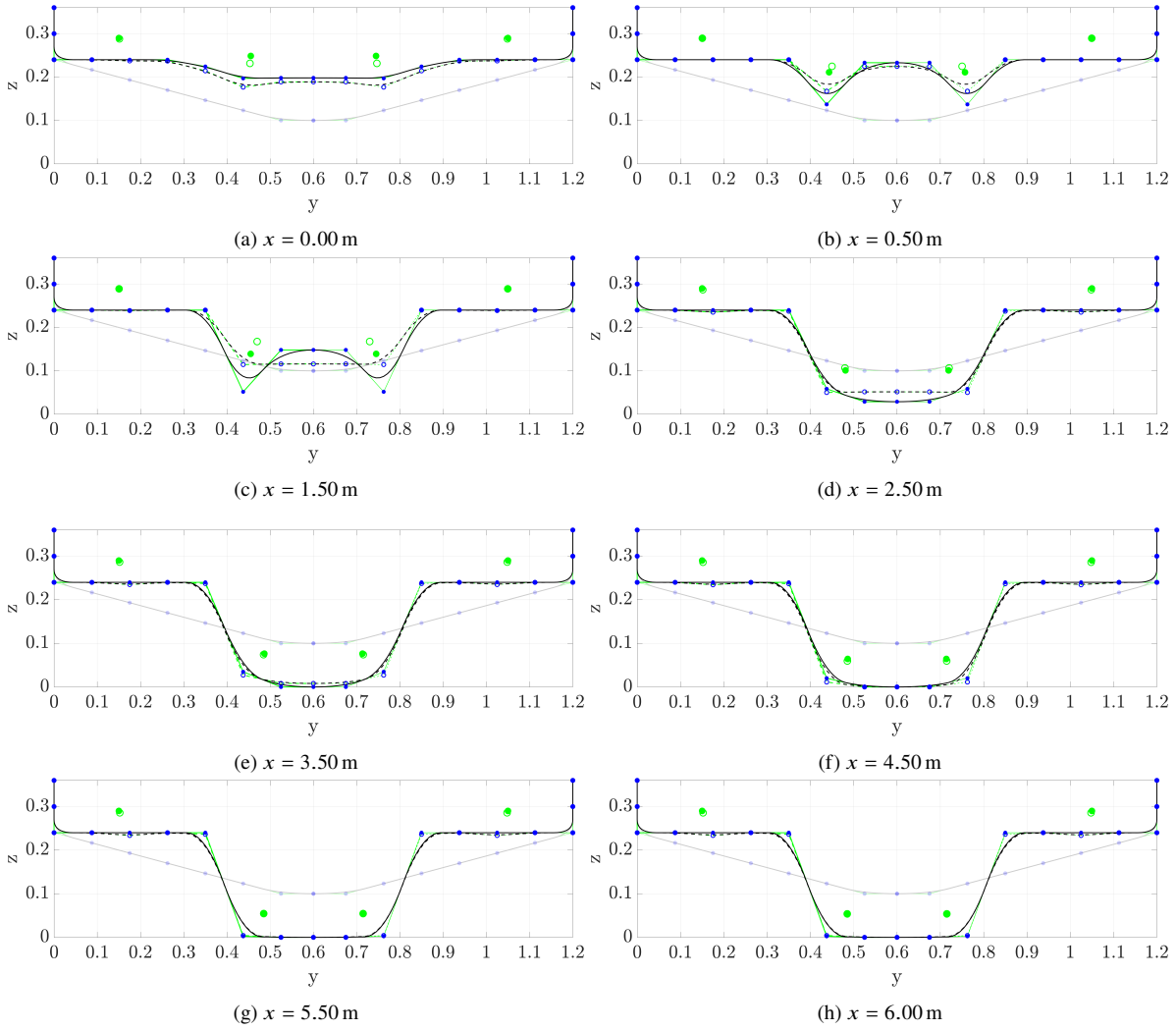

Figure 27: Control polygons and corresponding B-spline boundary curve in the cross-sectional direction for the slab example. Initial configuration (light colors); optimized case without the buildability constraint (dashed lines, control points shown as hollow blue circles and cables as hollow green circles); and optimized case with the buildability constraint (solid lines, control points shown as filled blue circles and cables as filled green circles).

bounds, within which modifying the outer surface has only a limited effect on the total toolpath length. Consequently, the design has relatively little flexibility to recover buildability through geometric adaptation alone, making the reduction in printing velocity the more dominant factor for satisfying the buildability constraint. Finally, the linear approximation of the toolpath length was evaluated in the same manner as for the beam example, using the toolpath length from the optimization without buildability. The identified parameters were $a = 4.60$ and $b = 0.73$ m and a comparison between the sampled toolpath lengths and their linear approximation is shown in Figure 30.

Quantitative overview

In Table 5, we summarize the key measures for the initial and optimized designs. The total scaled objective $\tilde{\phi}$ decreases from 1.000 in the initial design to 0.491 in the case without the buildability constraint, and to 0.680 when the constraint is activated. The weighted component

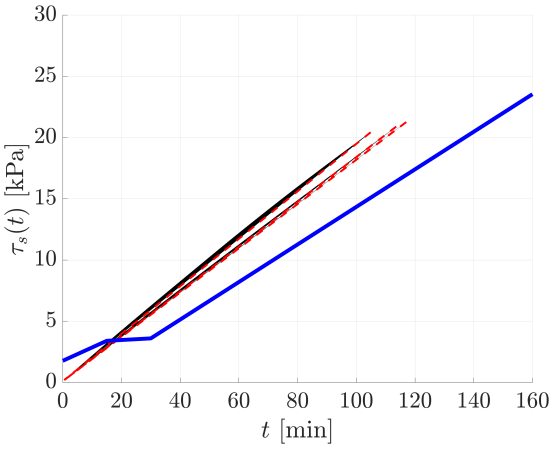

(a) 0% fiber

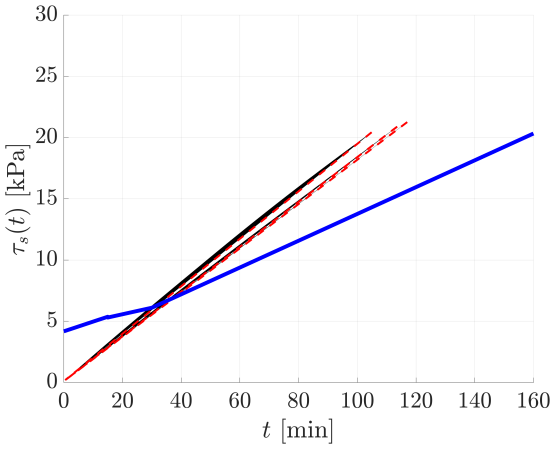

(b) 0.3% fiber

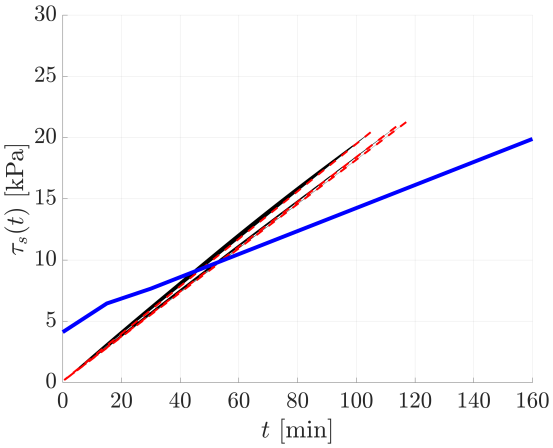

(c) 0.375% fiber

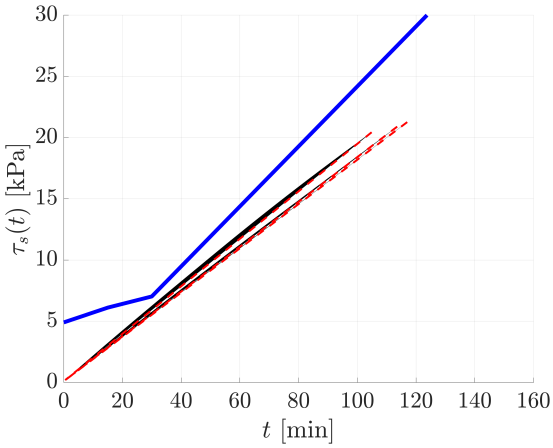

(d) 0.45% fiber

Figure 28: Buildup of layer stress and evolution of static yield stress over time for the examined mixtures. The blue line represents the material's static yield stress as a function of time, while the black lines indicate the cumulative stress in each layer. The dashed red lines highlight the accumulated stress in the first layers of the three segments.

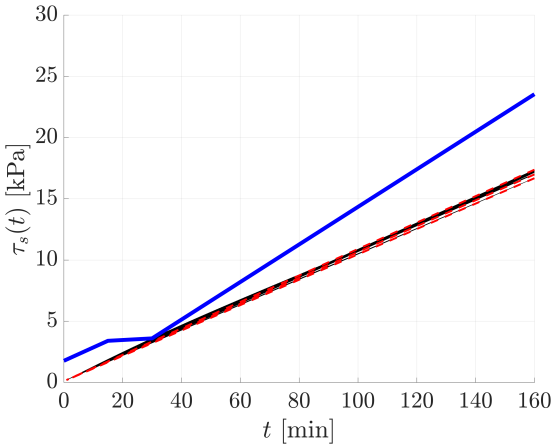

Figure 29: Buildability graph obtained by activating the buildability constraint for the fiber-free mixture. The blue line represents the material's static yield stress as a function of time, while the black lines indicate the cumulative stress in each printed layer.

associated with ϕ_1 is also reduced in the two optimized cases, demonstrating that the design

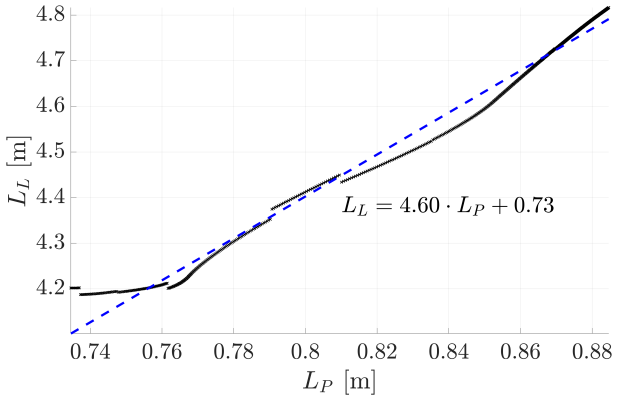

Figure 30: Linear approximation of the toolpath length per layer using parameters $a = 4.60$ and $b = 0.73$. Sampled values of the actual toolpath length are shown together with the corresponding linear fit.

becomes more balanced in terms of the absolute displacement along the upper chord. The reduction of the second objective indicates an increase in structural stiffness. Regarding the minimization of the prestressing forces governed by the third component of the objective, both cable groups start with the same initial prestressing force of 270 kN. In the case without the buildability constraint, the prestressing force in the side cables decreases to 182.63 kN, while the middle cable increases to its maximum value of 360 kN. When the buildability constraint is activated, the side cables reach 145.09 kN, whereas the middle cable again increases to its maximum value of 360 kN.

The fourth objective component, ϕ_4, represents the total printing time. The initial configuration requires approximately 6 h 56 min. In the case without the buildability constraint, this reduces to 5 h 37 min as the printing speed increases from 11 cm/s to the maximum allowable 15 cm/s. When the buildability constraint is activated, however, the printing time increases to about 9 h 57 min due to the reduced printing velocity of 8.63 cm/s. For the full structure, this corresponds to approximately 19 h 54 min.

The toolpath lengths in the full design for the two optimized cases are 6066.6 m and 6177.4 m, corresponding to printed material volumes of 1.21 m^3 and 1.24 m^3, respectively. Finally, all constraints are satisfied in both optimized cases, with their evaluated values converging toward zero.

Load-balancing effect

To further investigate the balancing effect of the prestressing, the displacement profiles along the mid-width upper chord of the slab, corresponding to the different combinations of applied forces, are shown in Figure 31. The maximum deformation associated with each load combination is reported in parentheses. The results shown correspond to the case in which the buildability constraint is activated. The maximum deformation due to self-weight and the balanced portion of the dead load, $\mathbf{u}_{s\tilde{d}} = -0.0386$ m, is largely counteracted by the prestressing deformation, $\mathbf{u}_p = +0.0345$ m, resulting in a combined displacement of $\mathbf{u}_{s\tilde{d}_p} = -0.0041$ m.

Measure	Initial	Optimized (without build.)	Optimized (with build.)
$\tilde{\phi}$	1.00	0.491	0.680
$w_1\ \phi_1/\phi_1^0$	0.3226	5.94e-03	2.23e-03
$w_2\ \phi_2/\phi_2^0$	0.3226	0.191	0.186
$w_3\ \phi_3/\phi_3^0$	0.03226	0.0324	0.0302
$w_4\ \phi_4/\phi_4^0$	0.3226	0.261	0.462
ϕ_1 [m^2]	3.796	7.01e-02	2.64e-02
ϕ_2 [kN·m]	0.382	0.226	0.220
ϕ_3 [kN]	540.0	542.63	505.09
ϕ_4	6h 56min	5h 37min	9h 57min
v [cm/s]	11.00	15.00	8.63
T_{sides} [kN]	270.00	182.63	145.09
T_{middle} [kN]	270.0	360.00	360.00
g_1	9.79e-02	-2.62e-05	-1.96e-05
g_2	3.09e-01	0	4.05e-04
N iteration	–	42	40

Table 5: Key measures for the initial and optimized slab designs.

The remaining load contributions, which are not required to be balanced, produce a maximum displacement of $\mathbf{u}_{\tilde{dl}} = -0.0229\,\text{m}$, leading to an overall maximum displacement of $\mathbf{u}_{spdl} = -0.0270\,\text{m}$.

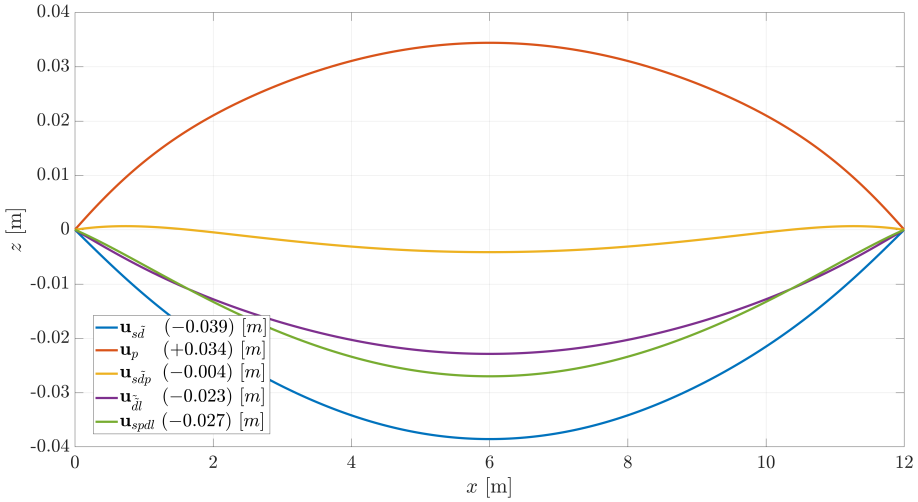

Figure 31: Deflections in the z-direction along the upper chord of the slab at mid-width for the different loading combinations.

Toolpath illustration

Finally, we illustrate the 3D-printed geometry of the optimized slab formwork, obtained with the buildability constraint. Figure 32 shows the 3D-printed layer profiles in the cross-sectional direction at several x-coordinates corresponding to the control points of the outer

surface. Figure 33 presents various views of the three printed segments that together form half of the slab span: a side view in Figure 33a, a bottom view in Figure 33b, and perspective views in Figures 33c and 33d.

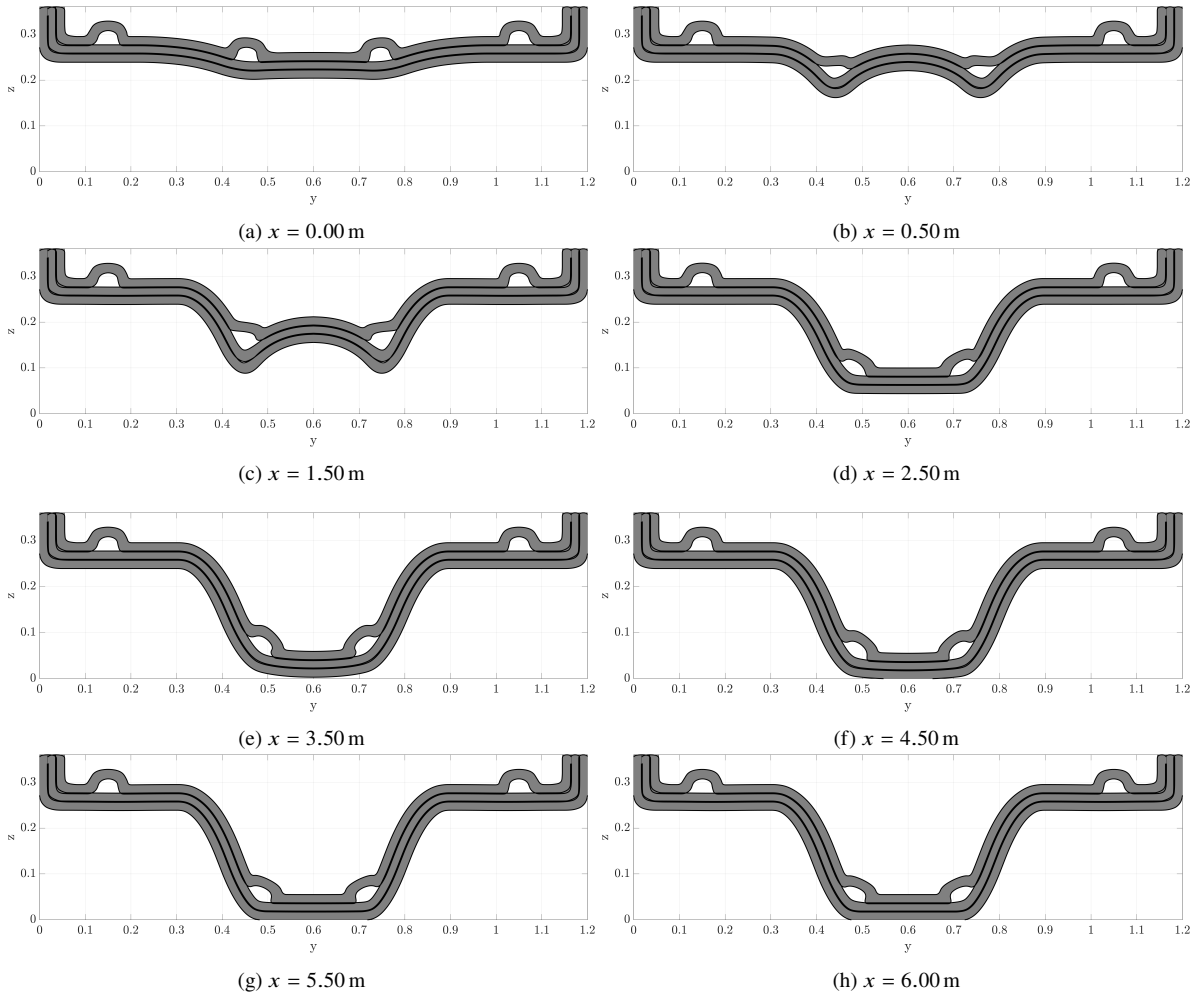

(a) $x = 0.00\,\text{m}$ (b) $x = 0.50\,\text{m}$

(c) $x = 1.50\,\text{m}$ (d) $x = 2.50\,\text{m}$

(e) $x = 3.50\,\text{m}$ (f) $x = 4.50\,\text{m}$

(g) $x = 5.50\,\text{m}$ (h) $x = 6.00\,\text{m}$

Figure 32: 3D-printed layers in the cross-sectional direction for the slab example optimized with the buildability constraint activated, corresponding to the x-coordinates of the control points on the outer surface.

10. Conclusions

This work presents a comprehensive, integrated methodology for the optimization of prestressed concrete structures under geometric, structural, buildability, and fabrication considerations. The framework combines structural performance objectives with practical constraints arising from additive manufacturing processes, thereby bridging the gap between computational design and physical realization. The proposed methodology is formulated for a two-stage fabrication approach, consisting of 3D-printed stay-in-place formwork followed by subsequent concrete casting, with prestressing introduced through post-tensioning during assembly. A layer-by-layer verification procedure based on the evolving shear strength of fresh concrete, together with geometric regularization constraints, enables the optimizer to generate shapes that

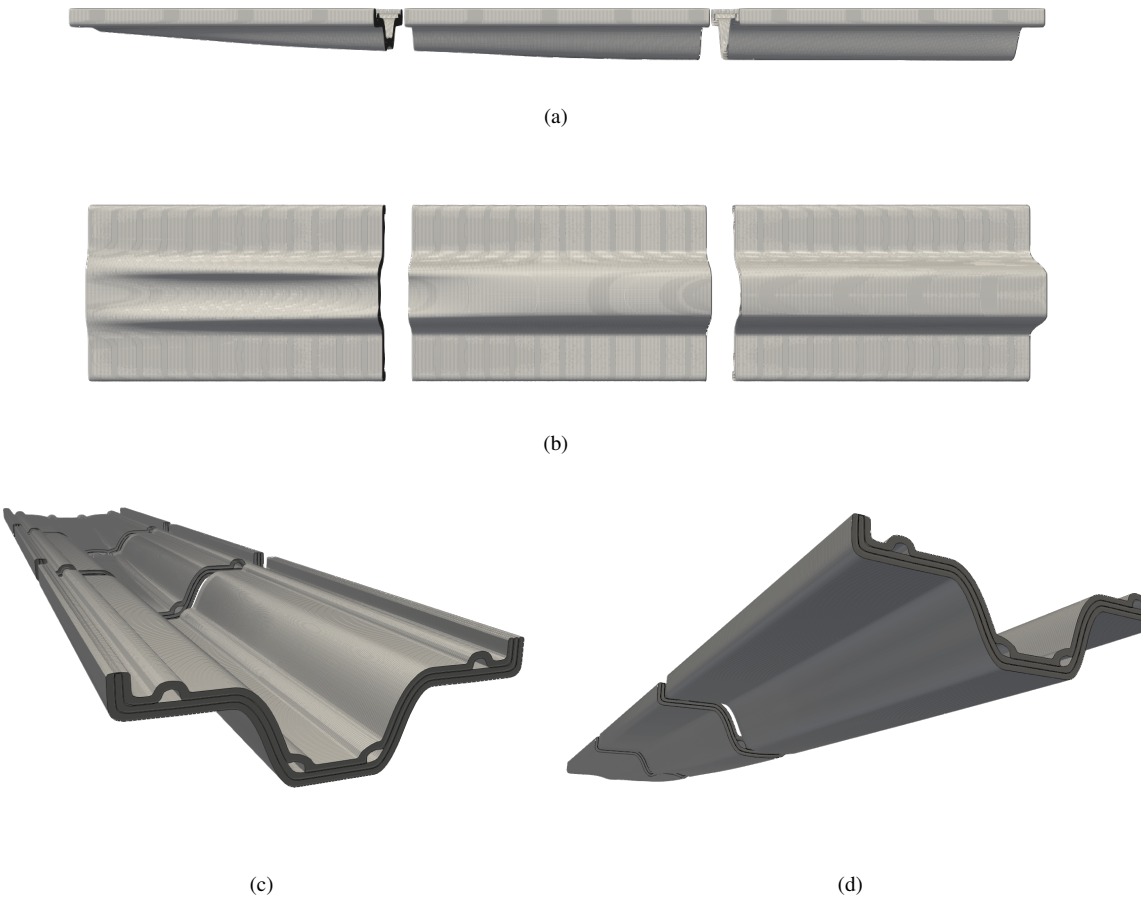

Figure 33: Different views of the 3D-printed slab segments. (a) Side view; (b) bottom view; (c) and (d) two different perspective views.

are simultaneously structurally efficient, manufacturable through 3D printing, and buildable with respect to early-age material behavior.

The methodology is demonstrated on two designs cases: a beam and a unidirectional slab. For each case, two optimization scenarios are examined—one without the buildability constraint and one with the constraint enforced. In the unconstrained cases, the optimizer successfully reduces the objective function and yields a geometrically efficient design; however, subsequent buildability analysis shows that such a design would fail under realistic printing conditions, particularly without fiber reinforcement or when higher printing speeds are applied. When the buildability constraint is activated, the optimization produces a modified geometry and a reduced printing velocity that together ensure manufacturability with a fiber-free mix. As expected, this leads to a higher printing time, because slower deposition allows the concrete to cure further and increase its yield strength before subsequent layers are placed. Nevertheless, the resulting solutions satisfy both structural and buildability requirements, underscoring the importance of embedding these constraints directly within the optimization framework. The study further investigates how segmentation strategies, material parameters, and printing velocity influence

buildability outcomes.

Overall, the proposed approach establishes a foundation for systematically integrating geometry, mechanics, and fabrication considerations in the design of 3D-printed prestressed concrete structures. Future work will extend the methodology in several directions, including the incorporation of additional process-dependent constraints, the consideration of staged prestressing during assembly—given that the final prestressing force may need to be applied gradually—and the development of more advanced buildability models. Experimental testing of the optimized designs will further support calibration of the formulation and help quantify the relative importance of each component. Taken together, these developments provide progress towards a holistic design-for-manufacturing strategy in 3D concrete printing, enabling the realization of highly optimized prestressed members with reduced material usage and embodied CO_2, while remaining practical to fabricate.

Acknowledgments

This work is part of the project AM2PM: Additive to Predictive Manufacturing for Multistorey Construction Using Learning by Printing and Networked Robotics. The project is funded by the European Union, under the program HORIZON-EIC-2023-PATHFINDERCHALLENGES-01. The support of the European Innovation Council is gratefully acknowledged.

Appendix A. Shear strength functions for different mixtures

In this appendix, we report the piecewise-defined functions describing the evolution of the shear strength, $\tilde{\tau}(t)$ (in Pa), for mixtures with different fiber contents. The corresponding parameters are extracted based on the work of (Asaf et al., 2024a,b). Each function is expressed in a piecewise linear form, where time t is measured in minutes.

Reference case (no fibers)

$$\tilde{\tau}(t) = \begin{cases} 108.960\,t + 1765, & t \leq 15 \text{ min}, \\ 13.200\,t + 3201, & 15 \text{ min} < t < 30 \text{ min}, \\ 153.432\,t - 1006, & t \geq 30 \text{ min}. \end{cases} \tag{A.1}$$

Cement + 0.3% fibers

$$\tilde{\tau}(t) = \begin{cases} 79.602\,t + 4170, & t \leq 15 \text{ min}, \\ 53.268\,t + 4502, & 15 \text{ min} < t < 30 \text{ min}, \\ 109.464\,t + 2816, & t \geq 30 \text{ min}. \end{cases} \tag{A.2}$$

Cement + 0.375% fibers

$$\tilde{\tau}(t) = \begin{cases} 156.000\,t + 4107, & t \leq 15 \text{ min}, \\ 80.802\,t + 5235, & 15 \text{ min} < t < 30 \text{ min}, \\ 94.068\,t + 4837, & t \geq 30 \text{ min}. \end{cases} \tag{A.3}$$

Cement + 0.45% fibers

$$\tilde{\tau}(t) = \begin{cases} 80.598\,t + 4901, & t \leq 15 \text{ min}, \\ 60.798\,t + 5198, & 15 \text{ min} < t < 30 \text{ min}, \\ 245.100\,t - 331, & t \geq 30 \text{ min}. \end{cases} \tag{A.4}$$

References

Amir, O., Shakour, E., 2018. Simultaneous shape and topology optimization of prestressed concrete beams. Structural and Multidisciplinary Optimization 57, 1831–1843. Publisher: Springer.

Andrew, R.M., 2019. Global CO2 emissions from cement production, 1928–2018. Earth System Science Data 11, 1675–1710. Publisher: Copernicus Publications Göttingen, Germany.

Anton, A., Reiter, L., Wangler, T., Frangez, V., Flatt, R.J., Dillenburger, B., 2021. A 3d concrete printing prefabrication platform for bespoke columns. Automation in Construction 122, 103467.

Asaf, O., Bentur, A., Amir, O., Larianovsky, P., Meyuhas, O.Y., Michli, E., Sprecher, A., 2024a. A 3d printing platform for design and manufacturing of multi-functional cementitious construction components and its validation for a post-tensioned beam. Materials 17, 4653.

Asaf, O., Bentur, A., Larianovsky, P., Sprecher, A., 2024b. Granular materials for 3d printing of construction components and structures. Automation in Construction 166, 105544.

Bai, M., Xiao, J., Ding, T., Yu, K., 2025. Interfacial bond properties between 3d printed engineered cementitious composite (ecc) and post-cast concrete. Cement and Concrete Composites 157, 105897.

Bhooshan, S., Bhooshan, V., Dell'Endice, A., Chu, J., Singer, P., Megens, J., Van Mele, T., Block, P., 2022. The Striatus bridge: Computational design and robotic fabrication of an unreinforced, 3D-concrete-printed, masonry arch bridge. Architecture, Structures and Construction , 1–23Publisher: Springer.

Chen, Y., Zhang, W., Zhang, Y., Zhang, Y., Liu, C., Wang, D., Liu, Z., Liu, G., Pang, B., Yang, L., 2023. 3d printed concrete with coarse aggregates: Built–in–stirrup permanent concrete formwork for reinforced columns. Journal of Building Engineering 70, 106362.

Coward, A., Sørensen, J.H., 2023. 3d printed concrete beams as optimised load carrying structural elements–the minimass beam, in: Structures, Elsevier. p. 105624.

Gebhard, L., Mata-Falcón, J., Anton, A., Dillenburger, B., Kaufmann, W., 2021. Structural behaviour of 3d printed concrete beams with various reinforcement strategies. Engineering Structures 240, 112380.

Hasani, A., Dorafshan, S., 2024. Transforming construction? Evaluation of the state of structural 3D concrete printing in research and practice. Construction and Building Materials 438, 137027. Publisher: Elsevier.

Jayathilakage, R., Rajeev, P., Sanjayan, J.G., 2020. Yield stress criteria to assess the buildability of 3D concrete printing. Construction and Building Materials 240, 117989. URL: https://www.sciencedirect.com/science/article/pii/S0950061819334427, doi:https://doi.org/10.1016/j.conbuildmat.2019.117989.

Kruger, J., Cho, S., Zeranka, S., Viljoen, C., Zijl, G.v., 2020. 3D concrete printer parameter optimisation for high rate digital construction avoiding plastic collapse. Composites Part B: Engineering 183, 107660. URL: https://www.sciencedirect.com/science/article/pii/S1359836819336923, doi:https://doi.org/10.1016/j.compositesb.2019.107660.

Kruger, J., Zeranka, S., Zijl, G.v., 2019. 3D concrete printing: A lower bound analytical model for buildability performance quantification. Automation in Construction 106, 102904. URL: https://www.sciencedirect.com/science/article/pii/S0926580519301852, doi:https://doi.org/10.1016/j.autcon.2019.102904.

Li, Y., Wu, H., Xie, X., Zhang, L., Yuan, P.F., Xie, Y.M., 2024. FloatArch: A cable-supported, unreinforced, and re-assemblable 3D-printed concrete structure designed using multi-material topology optimization. Additive Manufacturing 81, 104012. URL: https://www.sciencedirect.com/science/article/pii/S2214860424000587, doi:https://doi.org/10.1016/j.addma.2024.104012.

Mechtcherine, V., Bos, F.P., Perrot, A., da Silva, W.L., Nerella, V., Fataei, S., Wolfs, R.J., Sonebi, M., Roussel, N., 2020. Extrusion-based additive manufacturing with cement-based materials–production steps, processes, and their underlying physics: a review. Cement and Concrete Research 132, 106037. Publisher: Elsevier.

Mogra, M., 2023. Design optimization of building elements for manufacturing using 3D concrete printing. Master's thesis. Technion - Israel Institute of Technology.

Mohan, M.K., Rahul, A., De Schutter, G., Van Tittelboom, K., 2021. Extrusion-based concrete 3D printing from a material perspective: A state-of-the-art review. Cement and Concrete Composites 115, 103855. Publisher: Elsevier.

Perrot, A., Rangeard, D., Pierre, A., 2015. Structural built-up of cement-based materials used for 3D-printing extrusion techniques. Materials and Structures 49, 1–8. doi:10.1617/s11527-015-0571-0.

Piegl, L., Tiller, W., 2012. The NURBS book. Springer Science & Business Media.

Qiu, M., Sun, Y., Qian, Y., 2024. Interfacial bonding performance of 3d-printed ultra-high performance strain-hardening cementitious composites (uhp-shcc) and cast normal concrete. Journal of Building Engineering 82, 108268.

Raza, S., Manshadi, B., Sakha, M., Widmann, R., Wang, X., Fan, H., Shahverdi, M., 2025a. Load transfer behavior of 3d printed concrete formwork for ribbed slabs under eccentric axial loads. Engineering Structures 322, 119148.

Raza, S., Sakha, M., Hassan, Z., Manshadi, B., Wang, X., Fan, H., Dillenburger, B., Shahverdi, M., 2025b. Flexural behavior of stay-in-place load-bearing 3d-printed concrete formwork for ribbed slabs. Engineering Structures 338, 120531.

Roussel, N., 2018. Rheological requirements for printable concretes. Cement and Concrete Research 112, 76–85. URL: https://www.sciencedirect.com/science/article/pii/S000888461830070X, doi:https://doi.org/10.1016/j.cemconres.2018.04.005.

Sakha, M., Raza, S., Wang, X., Fan, H., Pichler, N., Shahverdi, M., 2026. Design optimization and assessment of stay-in-place 3d printed concrete formwork for slabs. Automation in Construction 181, 106572.

Salet, T.A.M., Ahmed, Z.Y., Bos, F.P., Laagland, H.L.M., 2018. Design of a 3D printed concrete bridge by testing. Virtual and Physical Prototyping 13, 222–236. URL: https://doi.org/10.1080/17452759.2018.1476064, doi:10.1080/17452759.2018.1476064. publisher: Taylor & Francis _eprint: https://doi.org/10.1080/17452759.2018.1476064.

Shakur, E., Shaked, A., Amir, O., 2024. Topology and shape optimization of 3D prestressed concrete structures. Engineering Structures 321, 118936. Publisher: Elsevier.

Suiker, A.S.J., 2018. Mechanical performance of wall structures in 3D printing processes: Theory, design tools and experiments. International Journal of Mechanical Sciences 137, 145–170. URL: https://www.sciencedirect.com/science/article/pii/S0020740317330370, doi:https://doi.org/10.1016/j.ijmecsci.2018.01.010.

Svanberg, K., 1987. The method of moving asymptotes - a new method for structural optimization. International Journal for Numerical Methods in Engineering 24, 359–373.

Vantyghem, G., Corte, W.D., Shakour, E., Amir, O., 2020. 3D printing of a post-tensioned concrete girder designed by topology optimization. Automation in Construction 112, 103084. URL: https://www.sciencedirect.com/science/article/pii/S0926580519305096, doi:https://doi.org/10.1016/j.autcon.2020.103084.

Vantyghem, G., Ooms, T., Corte, W.D., 2021. VoxelPrint: A Grasshopper plug-in for voxel-based numerical simulation of concrete printing. Automation in Construction 122, 103469. URL: https://www.sciencedirect.com/science/article/pii/S0926580520310499, doi:https://doi.org/10.1016/j.autcon.2020.103469.

Wan, Q., Wang, L., Huang, X., Wu, H., Sanjayan, J., Hashemi, J., Ma, G., 2025. Shape optimization based on isogeometric analysis for 3d concrete printing: A design method for printing-friendly structure. Engineering Structures 345, 121501.

Wang, L., Yang, Y., Yao, L., Ma, G., 2022. Interfacial bonding properties of 3d printed permanent formwork with the post-casted concrete. Cement and Concrete Composites 128, 104457.

Wangler, T., Lloret, E., Reiter, L., Hack, N., Gramazio, F., Kohler, M., Bernhard, M., Dillenburger, B., Buchli, J., Roussel, N., Flatt, R., 2016. Digital Concrete: Opportunities and Challenges. RILEM Technical Letters 1, 67–75. URL: https://letters.rilem.net/index.php/rilem/article/view/16, doi:10.21809/rilemtechlett.2016.16.

Wolfs, R., 2019. Structural failure during extrusion-based 3D printing processes. The International Journal of Advanced Manufacturing Technology 104, 1–20. doi:10.1007/s00170-019-03844-6.

Wolfs, R.J.M., Bos, F.P., Salet, T.A.M., 2018. Early age mechanical behaviour of 3D printed concrete: Numerical modelling and experimental testing. Cement and Concrete Research 106, 103–116. URL: https://www.sciencedirect.com/science/article/pii/S000888461730532X, doi:https://doi.org/10.1016/j.cemconres.2018.02.001.

Zhu, B., Nematollahi, B., Pan, J., Zhang, Y., Zhou, Z., Zhang, Y., 2021. 3d concrete printing of permanent formwork for concrete column construction. Cement and Concrete Composites 121, 104039.